Article

Constraining the Timing of Evolution of Shear Zones in Two Collisional Orogens: Fusing Structural Geology and Geochronology

Rodolfo Carosi [1,*], Chiara Montomoli [1], Salvatore Iaccarino [1], Beatriz Benetti [1], Alessandro Petroccia [1] and Matteo Simonetti [2]

1   Dipartimento di Scienze della Terra, Università di Torino, 10125 Turin, Italy;
    chiara.montomoli@unito.it (C.M.); salvatore.iaccarino@unito.it (S.I.); beatrizyuri.benettisilva@unito.it (B.B.);
    alessandrogiovannimichele.petroccia@unito.it (A.P.)
2   Servizio Geologico d'Italia, ISPRA, 00144 Rome, Italy; matteo.simonetti@isprambiente.it
*   Correspondence: rodolfo.carosi@unito.it

Abstract: In recent decades, constraining the timing of shear activity has been one of the main topics of research about the tectono-metamorphic evolution of orogenic belts. We present a review of a combined structural and geochronological approach to two major ductile regional shear zones, in two collisional orogens: the first one affecting the Variscan basement in northern Sardinia (Italy) and the External Crystalline Massifs of the Alps (East Variscan Shear Zone; EVSZ), and the second one deforming the medium- to high-grade rocks of the metamorphic core of the Himalaya (High Himalayan Discontinuity). High-resolution, texturally and chemically controlled monazite geochronology applied in separated shear zones of the Variscan belt allowed recognizing a similar timing of activity ranging between c. 340–330 and 300 Ma. This approach led to a better understanding of the evolution of the EVSZ, supporting a model where several branches were active according to a growth by linkage model. Following a similar approach, in situ U-Th-Pb analysis of monazite constrained the timing of top-to-the-S/SW shearing of a regional-scale High Himalayan Discontinuity in the Himalayan belt to between c. 28 Ma and 17 Ma. Earlier exhumation of the hanging wall was triggered by shear zone activity, whereas at the same time, the footwall was still experiencing burial with increasing P-T conditions. The timing of shearing of this shear zone fits with an in-sequence shearing tectonic model for the exhumation of the Himalayan mid-crust.

Keywords: collisional orogens; shear zone; petrochronology; U-Th-Pb geochronology

1. Introduction

Dating deformation events in tectonites and therefore unraveling the tectonic and structural evolution of the deformation of the lithosphere in different geodynamic settings are major challenges in structural geology [1–3]. Crosscutting relationships among structures such as folds, foliations and shear zones, magmatic bodies, unconformities and the stratigraphic age of the deformed sequence, as well as the age of sedimentary rocks deposited during or after deformation and magmatism, allow relative dating of major deformation events in the deformed lithosphere [4,5]. However, deformed rocks often show several episodes of superposed deformation and metamorphism such that the use of basic geological criteria often does not allow for an adequate temporal resolution. To overcome this problem, radiometric dating of mineral (re)crystallization within different fabrics has been widely used in folded and sheared rocks to better unravel the deformation history (e.g., [6,7]). In addition, in situ dating techniques enable retention of the structural positions of the minerals with respect to the different deformation structures to be dated. This approach allows full use of textural information regarding the relationships between rock-forming minerals and fabrics.

In the internal portions of orogenic belts, rocks usually suffer burial at very different pressure (P) and temperature (T) conditions followed by exhumation. During this complex path, deformation is closely associated with metamorphic processes [8] that are linked to the chemical composition of minerals reflecting prograde or retrograde reactions during changing P-T conditions, the strain rate and the presence or absence of fluids. Later retrograde processes often erase information about the initial history of the rocks, with re-equilibration of minerals at lower P-T conditions causing partial or complete loss of geological information about the early history. As a result, metamorphic minerals, both rock-forming and accessory, are rarely chemically homogeneous and show chemical zoning with respect to major and trace elements. Therefore, when dating minerals such as amphibole, mica, zircon, monazite and titanite, a large spread of ages is often obtained, even in a single mineral [9,10]. It is challenging to link the obtained ages to the structures recorded in the different deformation events recognized in the rock in the field and under the microscope. When dating key or index metamorphic minerals, it is easier to link the age to a deformation and metamorphic event (e.g., sodic amphibole for blueschist [11]). Difficulties increase when trying to link ages and deformation structures using minerals that are present under different P-T-X conditions, such as zircon, monazite and titanite [10,12–14]. However, the complexity in the age and mineral chemistry of accessory-phase geochronometers is the key to better unraveling the history of deformation and metamorphism in rocks. Recent approaches have combined in situ U-Th-Pb data with the geochemical composition of the minerals to establish the timing of geologic events [10]. In this contribution, we focus on monazite dating (e.g., [15]) in metapelites. Monazite, a Th-bearing REE phosphate, is currently considered a powerful and reliable geochronometer (e.g., [2,3,10,16,17]). This mineral could record the timing for a wide spectrum of metamorphic conditions, from the greenschist facies up to the granulite facies condition (e.g., [16–19]).

In situ monazite dating offers the possibility of linking absolute timing to chemical and/or microstructural domains related to metamorphic reactions and/or deformative events. In this contribution, we present a review including two examples of direct dating of regional-scale shear zones in ancient and modern orogenic belts from: (a) the Variscan belt in Southern Europe (Figure 1), and (b) the metamorphic core of the Himalaya (Figure 2).
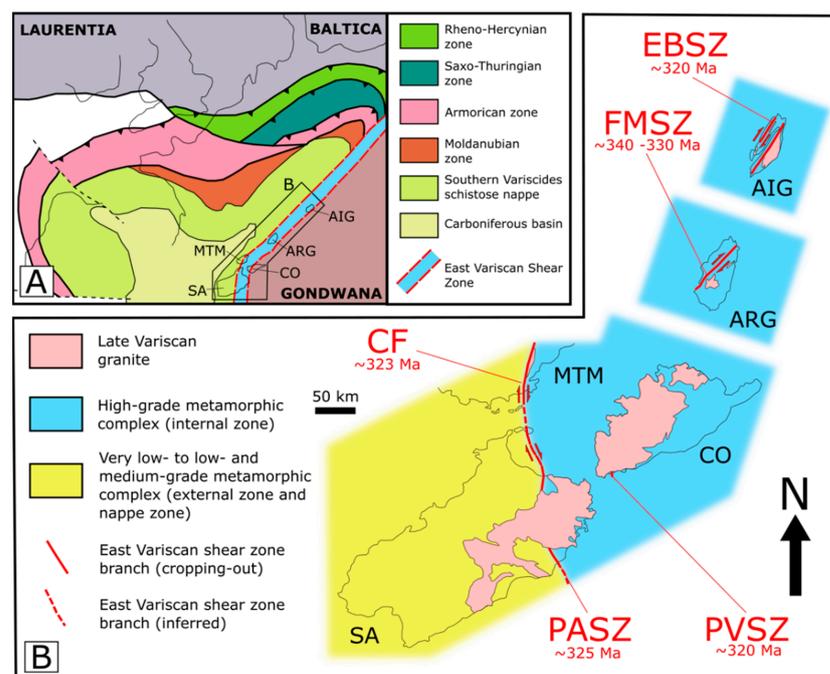

Figure 1. (**A**) Sketch maps of the Southern European Variscan belt during the late Carboniferous (modified from Faure et al., 2005 [20]; Corsini and Rolland, 2009 [21]; Guillot and Ménot, 2009 [22]); (**B**) inferred

lateral relationships between the branches of EVSZ during the late Carboniferous (modified from Simonetti et al., 2020 [23]). SA = Sardinia; MTM = Maures–Tanneron Massif; CO = Corsica; ARG = Argentera Massif; AIG = Aiguilles Rouge Massif; PASZ = Posada–Asinara Shear Zone; CF = Cavalaire Fault; PVSZ = Porto Vecchio Shear Zone; FMSZ = Ferriere–Mollières Shear Zone; EBSZ = Emosson–Berard Shear Zone.
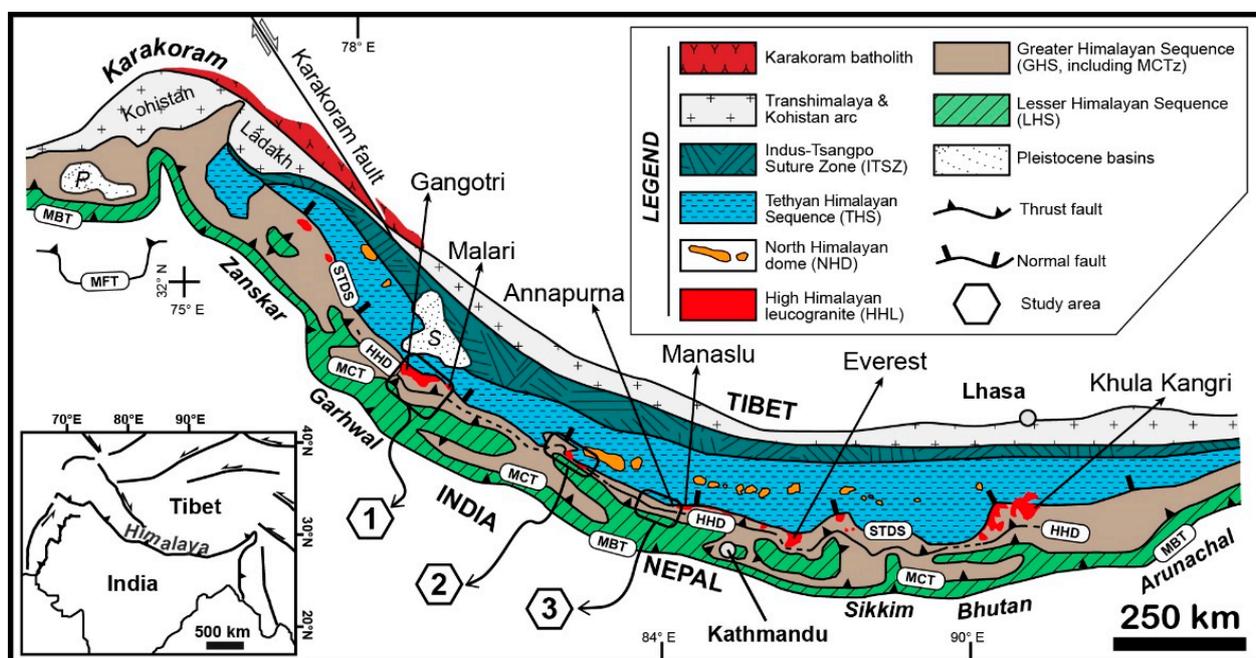

Figure 2. Geological map of the Himalaya (modified from Weinberg, 2016 [24]). Abbreviations: MFT, Main Frontal Thrust; MBT, Main Boundary Thrust; MCT, Main Central Thrust; HHD, High Himalayan Discontinuity; STDS, South Tibetan Detachment System; P, Peshawar basin; S, Sutlej basin. (1) Badrinath Shear Zone (NW India); (2) Tojiem and Mangri Shear Zones (west Nepal); (3) Chomrong Thrust (central Nepal).

2. Monazite Behavior during Metamorphism: A Synthesis

For a successful application of monazite geochronology to solve geological problems, an evaluation of the monazite-in reaction, as well as monazite growth/resorption compared with the tectono-metamorphic evolution of the study sample, is required [25–27]. It is fundamental to investigate the chemical changes of both rock-forming minerals and monazite (re)crystallization with respect to the P-T-D evolution of the studied rock (Figure 3).

Monazite may display different internal foliations analogous to porphyroblasts [27] or asymmetric growth tails during shearing [28]. A close link between the monazite age and chemical domain has often been reported, and rare-earth element (REE) + Y concentrations, coupled with U and Th zoning and variations in Eu anomalies, have been used as proxies to link monazite ages to different phases of metamorphism [2,26,29,30]. The behavior of monazite during metamorphism and partial melting has been extensively investigated both on the basis of empirical and experimental studies ([12] and references therein). Consequently, despite being far from complete, we have a reasonable understanding of monazite behavior and its chemical signature. These studies have shown that the distribution of Th, Y and heavy rare-earth elements (HREE) is strongly controlled by the coupled growth/dissolution of coexisting phases such as garnet, xenotime, apatite and/or allanite [12,25,31]. Common reactions forming monazite in the metamorphic assemblage during a prograde history of metapelites are related to the breakdown of allanite at ~450–550 °C, especially in relatively Ca-rich pelites (e.g., [32]). Garnet is regarded as the main silicate phase controlling the Y + HREE budget during monazite growth (e.g., [25,32]). Consequently, the initial growth of monazite (Figure 3) is expected to show higher Th and

HREE + Y contents due to the breakdown (up to the complete consumption) of allanite and/or xenotime [33]. During continuing prograde metamorphism (Figure 3), together with garnet growth, coexisting monazite should show lower Y + HREE concentrations [32,33].
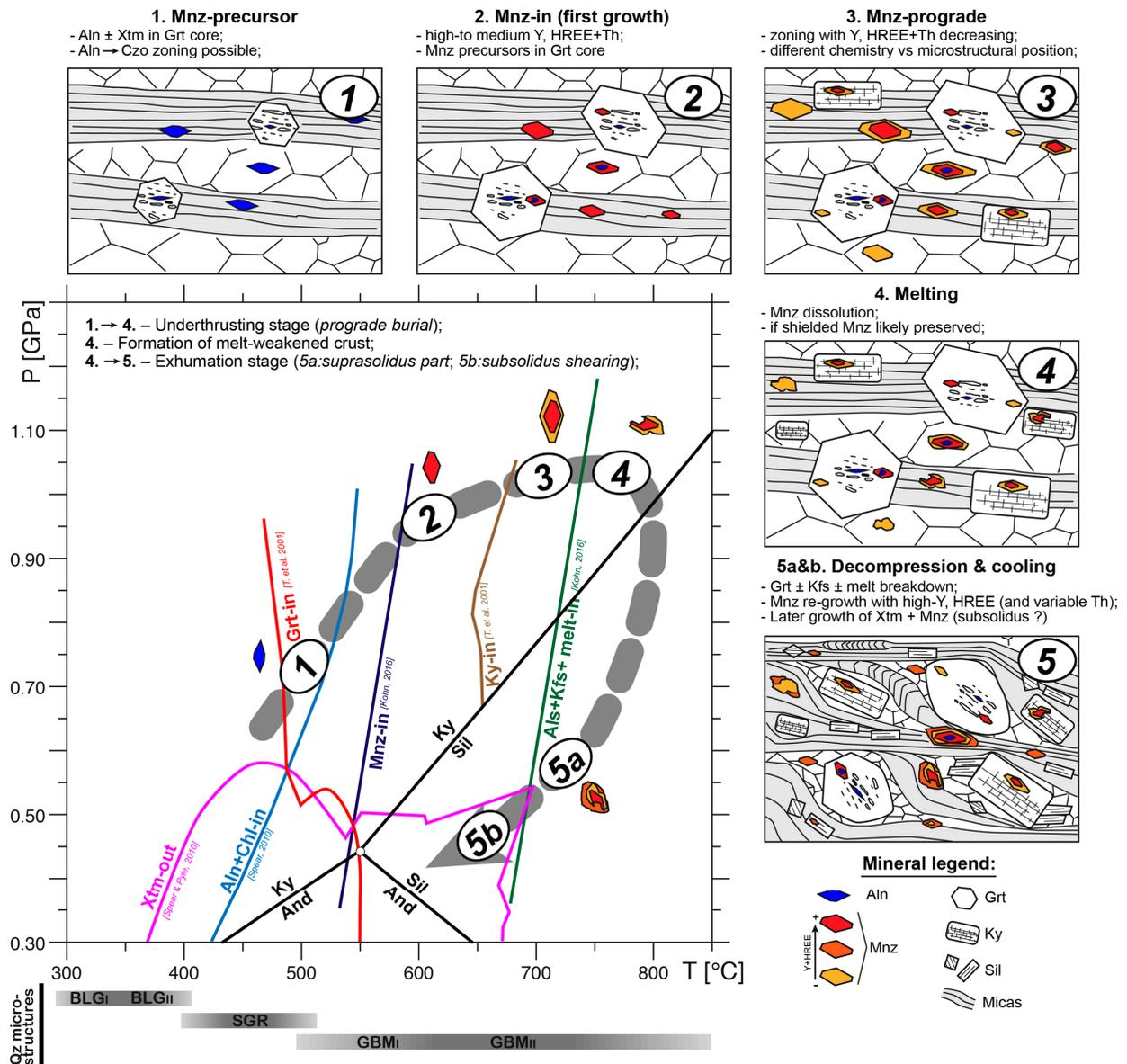

Figure 3. Simplified (and idealized) sketch showing the possible P-T-D evolution of a metamorphic tectonite vs. monazite behavior/zoning. Note that several complexities (e.g., fluids, different bulk compositions) can modify this picture. T range for quartz dynamic recrystallization mechanisms from Law (2014) [34] and Stipp et al. (2002) [35] (BLG—bulging recrystallization; SGR—subgrain rotation recrystallization; GBM—grain boundary migration recrystallization). Mineral-in curves: Als + Kfs + melt-in and Mnz-in = Kohn (2016) [10]; Grt-in and Ky-in = Tinkham et al. (2001) [36] (MnNCKFMASH system); Aln + Chl-in = Spear (2010) [37]; Xtm-out = Spear and Pyle (2010) [32]. Mineral abbreviations as in Whitney and Evans (2010) [38].

If, during prograde growth, garnet-consuming reactions occur (e.g., the appearance of staurolite), monazite domains should show an increase in Y + HREE. During partial melting, the high solubility of phosphate in the peraluminous melt results in monazite dissolution (Figure 3), whereas during crystallization of the melt by cooling and concomitant garnet breakdown, precipitation of high-Y + HREE monazite is expected (e.g., [26,30,39,40]).

Variation in Eu anomalies coupled with the Ca/Sr ratio, in a suprasolidus condition, can further help to link monazite ages to melt-present and/or feldspar growth/dissolution stages [41–43]. During further cooling, subsolidus HREE + Y-rich monazite (and xenotime) can be formed at the expense of the ongoing garnet (and fluid)-consuming reactions. From this summary, it is evident that the correlation of microstructural positions alone is no longer sufficient to interpret the tectonic significance of monazite ages [10]. Since the relative growth of rock-forming minerals (e.g., garnet, feldspars) or the crystallization of the melt can be "predicted" within the equilibrium thermodynamic framework (i.e., pseudosections), it is possible, in principle, to link monazite chemical fingerprints to a particular stage of the P-T-D path (e.g., [41–43]). Moreover, recent advances in experimental and theoretical work have also tried to include monazite in pseudosection modeling that, despite far from being perfect, is really promising (e.g., [31,32,44,45]).

3. Geological Setting of the Southern Variscan Belt

Between c. 380 Ma and 280 Ma [6,46–49], the continent–continent collision involving Laurentia–Baltica and Gondwana (Figure 1) led to the final assemblage of Pangea and to the development of the Variscan belt. It is represented by a 1000 km-wide and 8000 km-long mountain system that extends from the Caucasus to North America [49]. The main debate concerning the Variscan collision in Europe is about the presence or absence of microplates between Laurentia–Baltica and Gondwana [49,50].

The portion of the belt exposed in Central and Western Europe is known as the Variscides. The architecture of the belt in this sector has been defined by many authors [49,51–54]: the Saxothuringian Zone (southwestern Iberian Massif, northern Armorican Massif, Vosges and Bohemian Massif) and the Moldanubian Zone (southern Iberian Massif, central and southern Vosges, Massif Central, southern Armorican Massif and southern Bohemian Massif) (Figure 1). The latter is considered as the metamorphic root of the belt [55].

The Variscides are characterized by a composite orocline showing two large-scale arcs [56,57]: a western branch known as the Ibero-Armorican Arc [58–61] and a smaller eastern branch [23,49,62–65] delimited by a crustal-scale transpressional shear zone known as the East Variscan Shear Zone (EVSZ; [21,23,66–69]. According to Matte (2001) [49], García-Navarro and Fernández (2004) [70] and Pereira et al. (2008) [71], the Variscan belt formed and evolved in a manner analogous to the indentation model proposed for the evolution of the Himalaya [72,73].

The south-eastern sector of the Variscides underwent reworking and fragmentation during the Alpine Orogeny. In the present day, the correlation between the now dispersed sectors of the belt is still debated and is mostly based on lithological and stratigraphic affinities and paleomagnetic data ([74–77] and references therein).

4. The East Variscan Shear Zone

The EVSZ should be seen as a network of interconnected transpressive shear zones that display a similar tectono-metamorphic evolution [62]. In the present day, evidence of the EVSZ is represented by the shear zones occurring in the dispersed fragments of the Variscan belt in the Mediterranean area (Table 1), such as in the Corsica–Sardinia Block, in the Maures Massif in Southern France and in the Alpine External Crystalline Massifs (Figure 1).

The Variscan belt in Sardinia belongs to the Corsica–Sardinia Block. In northern Sardinia, the occurrence of a late-Variscan, dextral transpressive shear zone, the Posada–Asinara Shear Zone (PASZ; Figures 1, 4a, 5A and 6a,b; Table 1), located between the High-Grade Metamorphic Complex (HGMC) and the Low- to Medium-Grade Metamorphic Complex (L-MGMC), has been well documented by several authors [6,67,78–81]. The transpressive deformation linked to the PASZ activity was recently investigated in detail by Carosi et al. (2020) [67] and Graziani et al. (2020) [82] in the Baronie region.
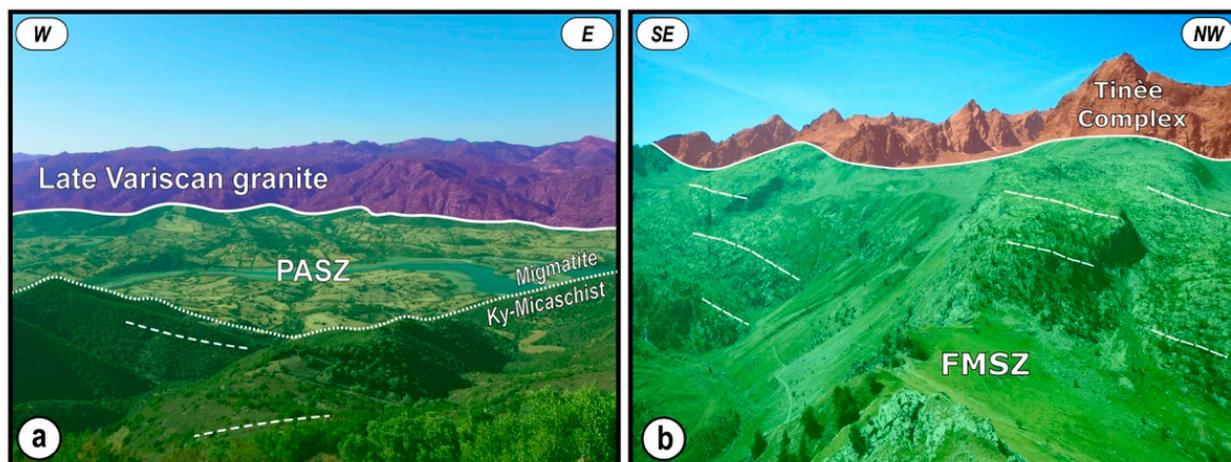
Figure 4. Panoramic view of two branches of the EVSZ, where the white dashed lines represent the orientation of the mylonitic foliation: (**a**) PASZ in northern Sardinia; (**b**) FMSZ in the Argentera Massif.
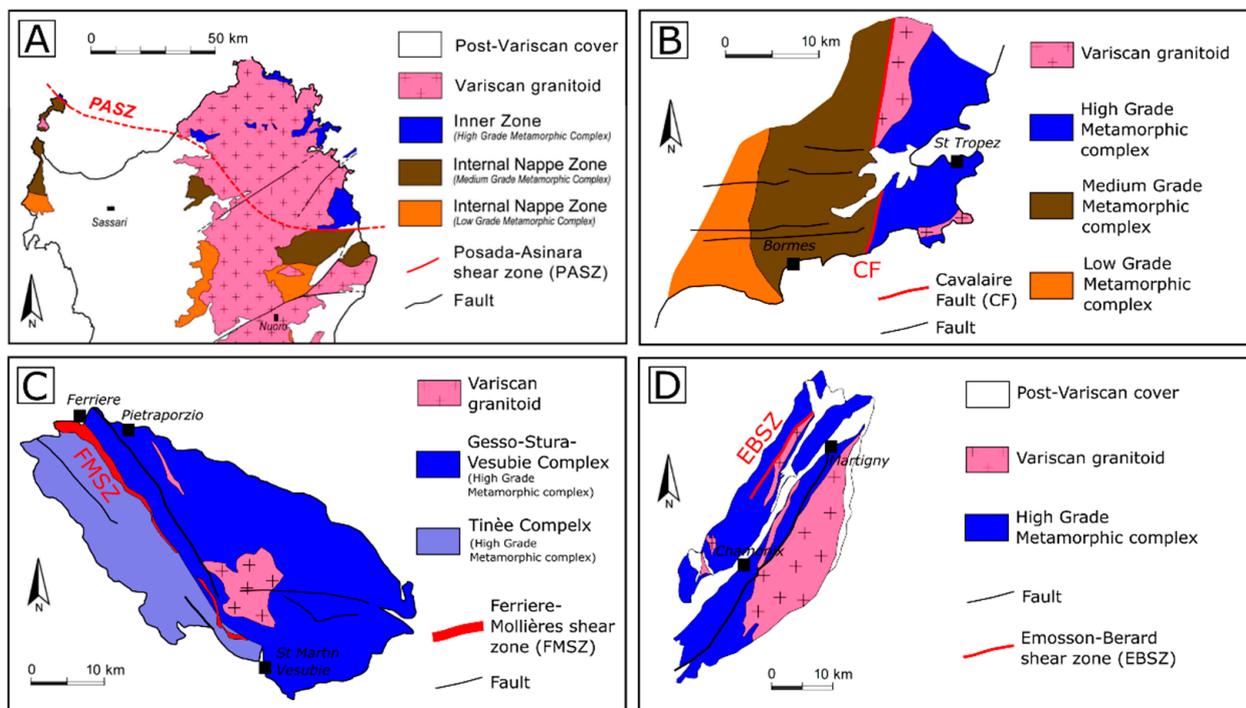

Figure 5. Schematic sketch maps of the Variscan fragments where segments of the EVSZ crop out: (**A**) northern Sardina; (**B**) Maures Massif; (**C**) Argentera Massif; (**D**) Aiguilles Rouge Massif.

Transpression affected the boundary between the HGMC and L-MGMC after collision-related deformation and metamorphism (D1 phase) [67,79]. An earlier HP event occurred in the HGMC ([83,84] with references), in metabasites of the PASZ [85] and in metapelites a dozen kilometers south of the PASZ [83]. The PASZ developed under decreasing temperature and pressure, from amphibolite facies conditions down to greenschist facies conditions [82–84] in the time span of ~25 Ma [66,67]. The amphibolite facies is confirmed by the presence of syn-kinematic sillimanite + biotite or biotite + white mica parallel to the mylonitic foliation [66,67]. This is also in agreement with the occurrence of GBM as the main dynamic recrystallization mechanism of quartz, indicative of temperatures higher than c. 500 °C. The presence of chlorite testifies to a decrease in the metamorphic conditions, supported by incipient SGR overprinting GBM in quartz [82].
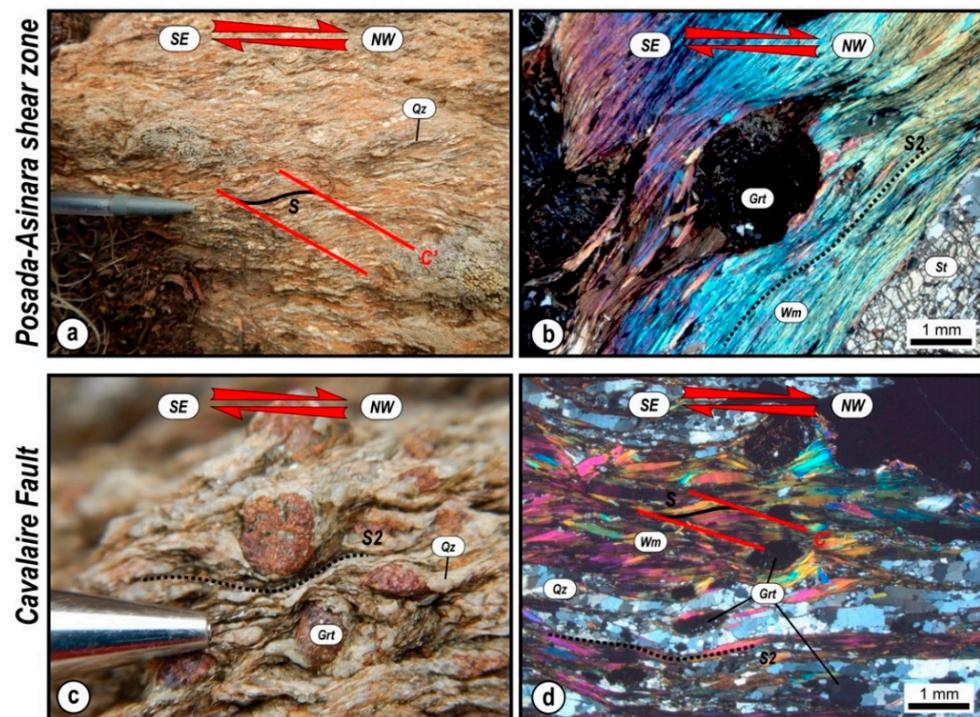
Figure 6. Evidence of shear deformation at the meso- and microscale of the PASZ and CF: (**a**) S-C′ fabric pointing to a top-to-the-NW sense of shear in the garnet-bearing micaschist; D2 transpressional deformation phase (coord. Lat 40°34′49.96″ N—Long. 9°15′37.30″ E) from the PASZ. (**b**) Asymmetric strain fringes around a garnet porphyroclast showing a top-to-the-NW sense of shear in staurolite-garnet-bearing micaschist (CPL) (coord. Lat 40°33′04.52″ N—Long. 9°24′38.00″ E) from the PASZ. (**c**) Asymmetric quartz strain fringes around a garnet porphyroclast in garnet-bearing micaschist showing a top-to-the-NW sense of shear; D2 transpressional deformation phase (coord. Lat 43°11′11.42″ N—Long. 6°35′11.22″ E) from the CF. (**d**) S-C′ fabric pointing a top-to-the-NW sense of shear in garnet-bearing micaschist (CPL) (coord. Lat 2°11′11.20″ N—Long. 6°35′11.50″ E) from the CF. Mineral abbreviations as in Whitney and Evans (2010) [38].

The PASZ displays a strong deformation gradient and strain partitioning, with the strain intensity increasing towards the N and a dextral top-to-the-W/NW sense of shear [66,67]. The PASZ developed under conditions of decreasing temperature, starting in amphibolite and evolving in greenschist facies conditions (D2 deformation phase [67]; D2 early and D2 late deformation phases [82]), as suggested by the changes in the syn-kinematic mineral assemblage and the shift in quartz recrystallization mechanisms [67,82]. The kinematic vorticity data highlight a transpressional deformation regime where the simple shear component of the flow increases along the deformation gradient (i.e., toward the N). The age of the PASZ has been constrained by monazite U-Th-Pb petrochronology [67]. Several monazite generations in different microstructural positions (along the mylonitic foliation or included in porphyroclasts) and with different chemical features and zoning were recognized. The first group is composed of grains with low- to medium-Y cores grown during the prograde D1 stage. The second group is composed of newly formed grains and rims around older monazite grains (that are not included in porphyroclasts) with a high Y content grown during the D2 phase. The last group includes low-Y rims formed during D3 around monazite grains that are not shielded by other phases. Analyses of monazite domains grown during the D2 transpression revealed that shearing along the PASZ started at ~325 and lasted up to ~300 Ma (Table 1).

In the Variscan portion of the MTM (Southern France; Table 1), the Cavalaire Fault (CF; [86]), a ductile shear zone, separates the High-Grade Complex to the east from the Medium-Grade Complex to the west (Figure 5B). The basement underwent HP conditions

linked to a complex and polyphase early collisional stage. HP is recorded in metabasite and meta-ultrabasite lenses embedded within migmatites. The CF initiated under amphibolite facies conditions. Schneider et al. (2014) [86] found that, in the transition zone of the Maures Massif, where the CF is localized, a retrograde metamorphism occurred between ~600° and ~400 °C. This is testified by miscrostructural observations such as the presence of GBM in quartz and syn-tectonic mineral assemblages along the mylonitic foliation such as Bt + Sill. Subsequently, deformation evolved under decreasing temperature conditions [62,86,87] testified by the partial and local overprint of GBM by SGR and by the growth of white mica. The CF is characterized by the presence of a mylonitic belt, similar to the PASZ, at the boundary between the External Zone and the Internal Zone (Figures 1, 5B and 6c,d). Recent kinematic vorticity analysis performed on sheared rocks of the CF revealed general shear conditions with a major component of pure shear acting together with simple shear under a dextral transpressional deformation regime [62]. The shear zone evolved under decreasing temperature conditions starting from amphibolite facies. To constrain the time of activity of the CF, several monazite generations in different microstructural positions (along the mylonitic foliation or included in porphyroclasts) and with different chemical features and zoning were analyzed. Monazite grains commonly show complex Y zoning [62]. In particular, three main compositional domains have been recognized: (1) high- to medium-Y cores; (2) low-Y cores; (3) high-Y rims. Monazites included in porphyroclasts do not show high-Y rims. The Y content in these grains decreases from the core to the rim. Monazites along the main foliation, or included in syn-kinematic minerals, generally present all three compositional domains or show a homogeneous high-Y composition. Dating of syn-tectonic high-Y domains of monazite grains revealed that shearing along the CF started at ~323 Ma [62] (Table 1).

Branches of the EVSZ in the Alpine External Crystalline Massifs occurring in the Western Alps are the Ferriere–Mollières Shear Zone (FMSZ; Figures 1, 4b and 5C; Table 1) in the Argentera Massif [88,89] and the Emosson–Berard Shear Zone (EBSZ; Figures 1 and 5D; Table 1) in the Aiguilles Rouge Massif ([23] with references). In the alpine basement, HP rocks also occur. They are mainly mafic eclogites embedded within migmatites. HP metamorphism occurred at ~341 Ma in the Argentera Massif (U-Pb on zircon [90,91]) and around ~345 Ma (U-Pb on zircon [92]) down to ~335–330 Ma (U-Pb on zircon and rutile [93]) in the Aiguilles Rouge Massif.

The FMSZ is a dextral shear zone (Figure 7a,b) and separates two migmatitic complexes: the Gesso Valle Stura Vesubiè to the NE and the Tiné Complex to the SW. The FMSZ shows a subvertical attitude and extends for about 20 km with a variable thickness between 100 m and more than 1000 m. Deformation along the FMSZ started shortly after peak metamorphism in the migmatite [94]. The FMSZ evolution is characterized by a type II growth [95] under different thermal stages recognized by quartz c-axis thermometers, microstructures and syn-tectonic mineral assemblages. The shear zone started at a temperature above ~600 °C and evolved under decreasing temperature down to ~400 °C.

Carosi et al. (2016) [96] recognized that the FMSZ shows a well-developed deformation gradient, with the strain intensity increasing from the wall rocks towards the center of the shear zone along with a gradual transition from protomylonite up to ultramylonite. Quartz opening-angle thermometers and syn-tectonic mineral assemblages suggest a decreasing temperature during deformation from HT amphibolite facies down to greenschist facies [94]. Kinematic vorticity analysis revealed a transpressional deformation with a prevalent pure shear component and a variable component of simple shear along the deformation gradient [63,94] (Table 1).
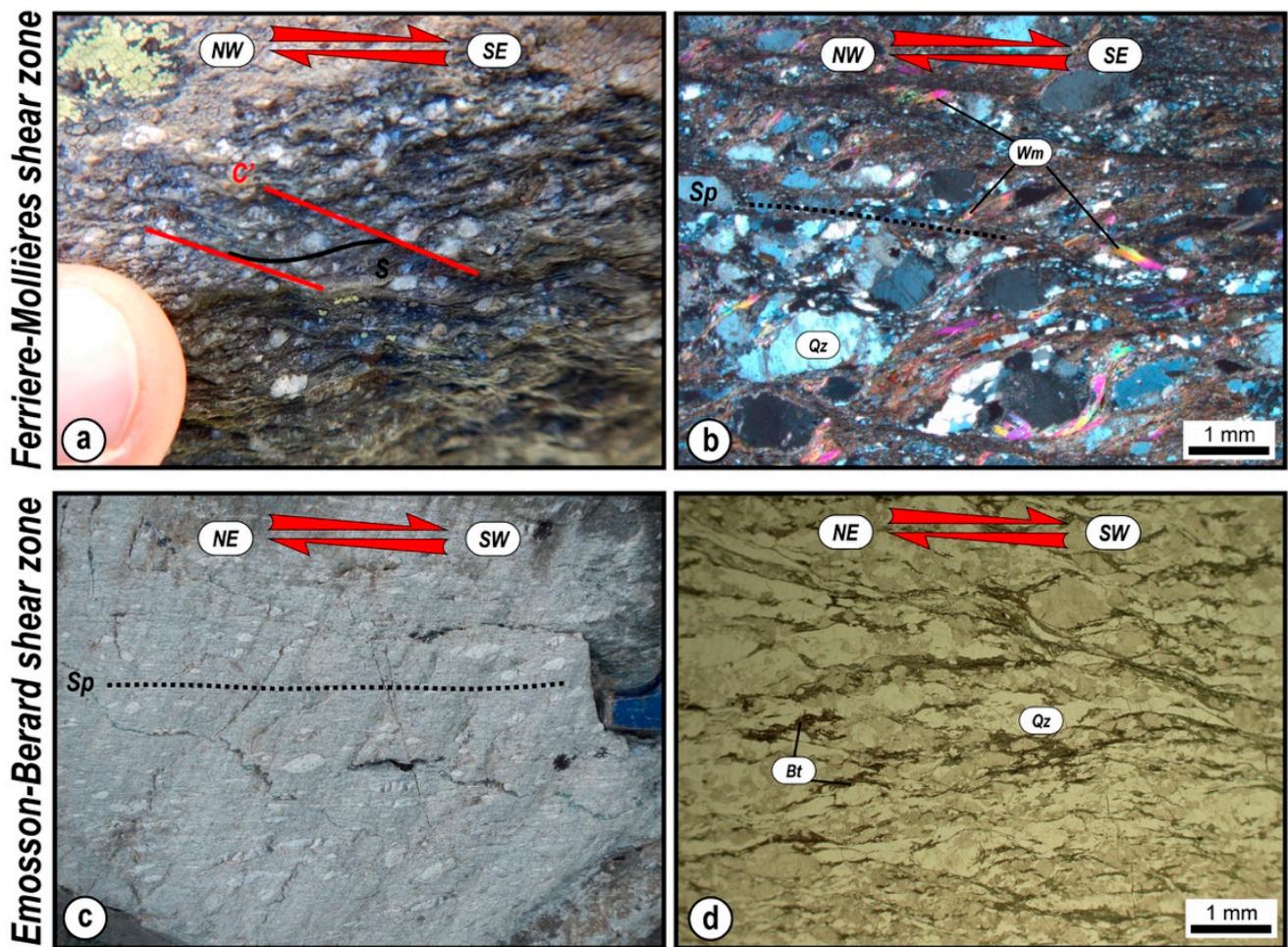
Figure 7. Evidence of shear deformation at the meso- and microscale of the FMSZ and of the EBSZ: (**a**) Mylonite at the outcrop-scale showing an S-C′ fabric indicative of a top-to-the-SE sense of shear; Sp is the mylonitic foliation (coord. Lat 44°18′23.90″ N—Long. 6°59′38.40″ E); FMSZ. (**b**) S-C-C′ fabric, mica fish and asymmetric porphyroclasts at the microscale showing a top-to-the-SE sense of shear (coord. Lat 44°18′23.90″ N—Long. 6°59′38.40″ E); FMSZ (CPL). (**c**) σ-type K-feldspar porphyroclast of centimetric size in sheared orthogneiss; Sp is the mylonitic foliation (coord. Lat 46°00′19.55″ N—Long. 6°51′56.15″ E); EBSZ. (**d**) Anastomosing disjunctive foliation in orthogneiss showing S-C′ fabric pointing to a top-to-the-SW sense of shear in mylonite (coord. Lat 46°03′55.00″ N—Long. 6°55′30.00″ E); EBSZ (PPL).

Table 1. Summary of structural and geochronology data sets of the branches of the EVSZ in the Mediterranean area [23,62,63,66,67,78,86,94,96].

Shear Zone and Locality	Variscan Tectonic Domains	Sheared Lithotypes	Strike & Dip of Mylonitic Foliation	Trend & Plunge of Lineation	Sense of Shear	Syn Shear Metamorphism	Deformation Mechanisms and Deformation T	Flow Regime	Timing	Syn-Tectonic Monazite Features
PASZ (Sardinia)	Internal and External Zones (HGMC/MGMC) [a]	Medium- to high-grade schist, gneiss, and migmatite [a,c]	S2: subvertical oriented E-W [a,c]	L2: oriented E-W with a variable plunging from subhorizontal to subvertical [a,c]	top-to-the-NW [a,c]	Retrometamorphism from Amphibolite-facies to greenschist-facies [a]	GBM to SGR in quartz; T variable from ~600° to ~400° C [b,c]	pure shear dominated transpression to simple shear dominated transpression [a,b,c]	325–300 Ma [c]	chemically homogeneous grains (high-Y) or zoned with a low-Y core and high-Y rim, sometimes a thin late low-Y rim is present [c]
CF (Maures Massif)	Internal and External Zones (HGMC/MGMC) [d,e]	Medium- to high-grade schist, gneiss, and migmatite [e]	S2: subvertical oriented NNE-SSW or dipping at medium angle toward the WNW [e]	L2: oriented NW-SE and plunging at medium angle toward WNW [e]	top-to-the-NW [e]	Retrometamorphism from Amphibolite-facies to greenschist-facies [d,e]	GBM in quartz; T between ~550° and 615° C [e]	pure shear dominated transpression [e]	323 Ma [e]	chemically homogeneous grains (high-Y) or zoned with a low-Y core and high-Y rim [e]
FMSZ (Argentera Massif)	Internal Zone (Tinèe and Gesso-Stura-Vesubie complexes) [f,g]	Migmatite [f]	S2: subvertical oriented NW-Se [f,g,h]	L2: oriented NW-SE subhorizontal or moderately plunging toward the NW [f,g,h]	top-to-the-SE [f,g,h]	Retrometamorphism from HT Amphibolite-facies to greenschist-facies [g,h]	GBM to SGR in quartz; feldspars fractured in lower grade mylonite; T variable from ~650° to ~400° C [h]	pure shear dominated transpression to simple shear dominated transpression [g,h]	340/330–305 Ma [g,h]	chemically homogeneous grains (high-Y) or zoned with a low-Y core and high-Y rim [g,h]
EBSZ (Aiguilles Rouge Massif)	Internal Zone [i]	Medium- to high-grade schist, gneiss, and migmatite [i]	Sp: subvertical oriented NE-SW [i]	Lp: oriented NE-SW and plunging toward the NE at low angle [i]	top-to-the-SW [i]	Retrometamorphism from Amphibolite-facies to greenschist-facies [i]	GBM to local incipient SGR in quartz; T variable from ~650° to ~550° C [i]	pure shear dominated transpression [i]	320 Ma [i]	chemically homogeneous grains (high-Y) or zoned with a low-Y core and high-Y rim [i]

[a]: Carosi & Palmeri, 2002; [b]: Carosi et al., 2012; [c]: Carosi et al., 2020; [d]: Schneider et al., 2014; [e]: Simonetti et al., 2020 [62]; [f]: Carosi et al., 2016; [g]: Simonetti et al., 2018; [h]: Simonetti et al., 2021; [i]: Simonetti et al., 2020 [23].

In order to unravel the timing of deformation, monazite grains, in different microstructural positions (included in porphyroclasts or along the mylonitic foliation), from the sheared rocks of the FMSZ were characchterized [63,94]. The Y content and zoning revealed that grains along the mylonitic foliation usually have a low-Y core, developed during the prograde stage of metamorphism, surrounded by a high-Y rim formed during syn-shear retrometamorphism. Some grains have an asymmetrical shape with the high-Y domains developed in the extensional sites around the grain. Differently, newly formed syn-tectonic grains present a homogeneous high-Y composition. Monazite included within porphyroclasts was shielded, and no high-Y rims are present. The ages obtained from syn-tectonic high-Y domains and grains revealed that shearing started at ~340–330 Ma in the protomylonites at the margins of the FMSZ. From mylonites, ages of ~320 Ma were obtained, suggesting a progressive concentration of the deformation in the core of the shear zone [63,94].

In the Aiguilles Rouge Massif, a detailed study of the EBSZ [23,97] revealed that it is a subvertical, high-strain mylonitic zone, developed in metasediment and orthogneiss, accommodating a pure-shear-dominated transpressional deformation (Figures 5D and 7c,d).

The deformation temperatures of the EBSZ were recently determined using a quartz c-axis opening-angle thermometer (temperature between ~630 °C and ~550 °C [23]) supported by microstructures and syn-tectonic mineral assemblages along the mylonitic foliation. The data suggest that deformation occurred under amphibolite facies conditions. Subsequently, deformation was active under lower temperature conditions even if it is difficult to clearly separate the low-T activity of the Variscan Shear Zone and the Alpine overprint/reactivation [23]. The age of deformation of the EBSZ was obtained by U-Th-Pb monazite petrochronology. According to the microstructural position, dated monazites are divided in two groups: the first group is represented by grains included in porphyroclasts (garnet or biotite), and the second group includes grains located along the mylonitic foliation [23]. The two groups differ in terms of chemical characteristics: the Y content is low in monazite included in porphyroclasts, while it is higher in grains located along the main foliation. From high-Y syn-tectonic monazites along the mylonitic foliation, ages between 320 Ma and 310 Ma were obtained, suggesting that shearing started at ~320 Ma [23] (Table 1).

Therefore, the timing of shearing along the PASZ (Figure 8a), the CF (Figure 8b), the FMSZ (Figure 8c) and the EBSZ (Figure 8d) is well constrained thanks to detailed data obtained from in situ texturally controlled U–(Th)–Pb geochronology on monazite [23,62,63,66,67,94]. The microstructural position, texture, zoning and chemical analyses highlight a complex history of monazite growth during the tectono-metamorphic history. Several generations of grains and chemical domains have been recognized. In general, monazite cores and grains included within porphyroclasts preserve older ages, between c. 340 and 333 Ma (Figure 8), that can be linked to the early collisional stage (between c. 380 Ma and 330 Ma; [98]) during the nappe stacking and prograde metamorphism. On the contrary, the growth of monazite rims around older cores or the growth of new homogeneous grains along the mylonitic foliation is linked to the decompression and retrogression stages that occurred during the transpressional phase of deformation. From those chemical domains and grains, ages of shearing between c. 340–330 Ma and 320 Ma have been obtained (Figure 8). Even if a detailed and complete study is not available at the moment, evidence of transpressional deformation has also been documented in the Belledonne Massif by Grandjean et al. (1996) [99], recognizing a transpressional deformation regime dated to 324 ± 12 Ma (K-Ar on hornblende), in agreement with the chronological data of the branches of the EVSZ. The chronological data obtained from in situ high-resolution monazite geochronology allow better constraining the progressive evolution over time of different branches of shear zones within a crustal-scale system—the EVSZ—in agreement with a growth by linkage model [94].
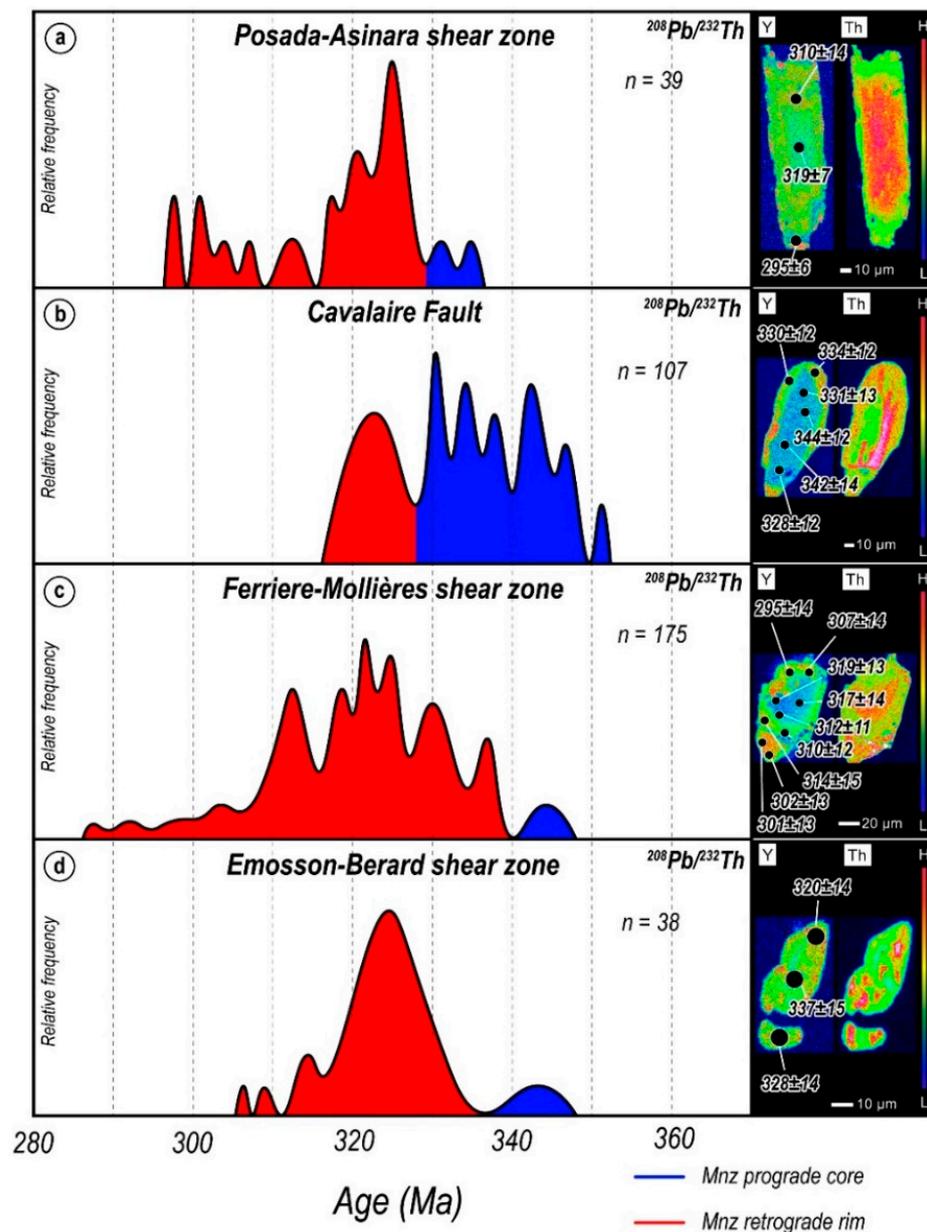
Figure 8. Probability density plot for ^{208}Pb/^{232}Th ages on monazite obtained from the study branches of the EVSZ. Blue and red fields represent the prograde and retrograde monazite-recorded history, respectively. Representative zoned monazite grains selected for in situ dating with the ^{208}Pb/^{232}Th relative date with its uncertainties are displayed. The color bar scale qualitatively shows lower (L) to higher (H) Y and Th concentrations. (**a**) Geochronological results from the PASZ (data from Carosi et al., 2020 [67]); (**b**) geochronological results from the CF (data from Simonetti et al., 2020 [62]); (**c**) geochronological results from the FMSZ (data from Simonetti et al., 2018, 2021 [63,94]; (**d**) geochronological results from the EBSZ (data from Simonetti et al., 2020 [23]).

5. Geological Setting of the Himalaya

The Himalayan belt (Figure 2) developed following the collision between the Indian and Eurasian Plates at ~59 Ma [100]. The tectonic units derived from the northern Indian Plate were stacked, building up the highest mountains in the world (Figure 2). Deeply metamorphosed rocks occur in the Greater Himalayan Sequence (GHS), a 3–30 km-thick sequence of medium- to high-grade metasedimentary and meta-igneous rocks. The lower part of the GHS is composed of garnet- to kyanite-bearing paragneiss and micaschist with subordinate calc-schist, quartzite, impure marble and migmatite. The middle portion of

the GHS is composed of calcsilicate gneiss and marble with minor pelitic and psammitic rocks. The uppermost part of the GHS consists of orthogneiss and aluminosilicate-bearing migmatitic rocks. The GHS is intruded by Oligo-Miocene leucogranites [24]. The Lesser Himalayan Sequence (LHS) and Tethyan Himalayan Sequence (THS) lay, respectively, structurally below and above the GHS. These sequences were formerly deposited on the Indian passive margin [101].

The GHS is bounded by a northward-dipping wide shear zone, the Main Central Thrust (MCT), separating it from the LHS [102,103], and by the South Tibetan Detachment System (STDS) separating it from the upper THS [104–107] (Figure 2). High-strain zones occur within the GHS and have been classically interpreted as out-of-sequence thrusts, affecting the GHS after a southward motion of the MCT ([108] and references therein).

The discovery of the contemporaneous activity of the normal-sense STDS at the top of the GHS and of the reverse-sense MCT at its base [106,109] had major consequences for formulating tectonic models for the exhumation of the mid-crust and led to the proposal of the following models: (i) channel flow [110], (ii) wedge extrusion [109,111], (iii) channel flow followed by wedge extrusion ([112,113] with references), (iv) wedge insertion [114] and (v) critical taper wedge [115]. All these models, except for (v), require the contemporaneous activity of the MCT and STDS to exhume the GHS between ~23 and 16 Ma ([112,116] with references).

6. High Himalayan Discontinuity in Western and Central Himalaya

The GHS records deformation associated with prograde and retrograde metamorphic events ([117–119] with references). Deformation is heterogeneously partitioned, and portions affected by folds and related foliations are separated by portions affected by discrete shear zones. The prominent fabric in the GHS is a transpositive foliation formed during a second deformation phase (D2; [120–122]). The S2 foliation strikes NW–SE and dips 30–60° toward the NE. It is marked by the preferred orientation of medium- to high-grade metamorphic minerals and recrystallized quartz ribbons. Kyanite, staurolite, muscovite and biotite are occasionally bent or kinked along shear bands. Sillimanite is frequently stretched within shear bands. Grain and aggregate lineations [4] (L2) trend NE–SW and plunge NE moderately to steeply (20°, 60°). The S1 foliation is preserved as a relict in S2 microlithons or as an internal foliation in porphyroblasts.

The HHD has been studied in detail in Nepal and NW India (Figures 2, 9 and 10) following a structural, petrological and petrochronological approach (Table 2).

Two main shear zones have been mapped in western Nepal at the same structural level in the GHS (Figures 2, 9 and 11): the Toijem [120,123] and the Mangri [116,120,124] Shear Zones. The mylonite thickness varies from a few dozen meters up to 4 km. In central Nepal, a shear zone has been recognized at the same structural level in the Kali Gandaki valley, named the Chomrong "Thrust" [125,126] (Figures 2 and 10a; Table 2). These three shear zones are localized in the lower portion of the GHS, close to the boundary between migmatite and kyanite-bearing gneiss, with hanging wall rocks showing a higher degree of melting than the footwall rocks. These structures are interpreted to be strands of the same high-temperature shear zone and are referred to as the HHD, showing a regional-scale occurrence [116,127].

In Garhwal Himalaya (NW India), the Badrinath Shear Zone mainly affects sillimanite-garnet-bearing gneiss of the GHS (Figures 2 and 10a; Table 2), showing former evidence of partial melting. The shear zone shows a hectometric thickness [128]. Shear sense indicators in the HHD, such as C-S fabric, shear bands, asymmetric tails around porphyroclasts, mica fish, asymmetric boudins and rotated garnets, indicate a top-to-the-S/SW sense of shear (Figure 11a–f). Shear planes dip to the N/NE, and the related object lineation plunges to the N/NE; these are inferred to be contractional shear zones. Quartz in mylonite shows evidence of high-T grain boundary migration (GBMII) recrystallization with often chessboard extinction [34]. Feldspar shows evidence of ductile deformation by undulose extinction, deformation twins and myrmekite. Deformation microstructures in the mylonite

suggest a high-temperature deformation regime (T > 650 °C; [4]), in agreement with the syn-kinematic growth of sillimanite + biotite.
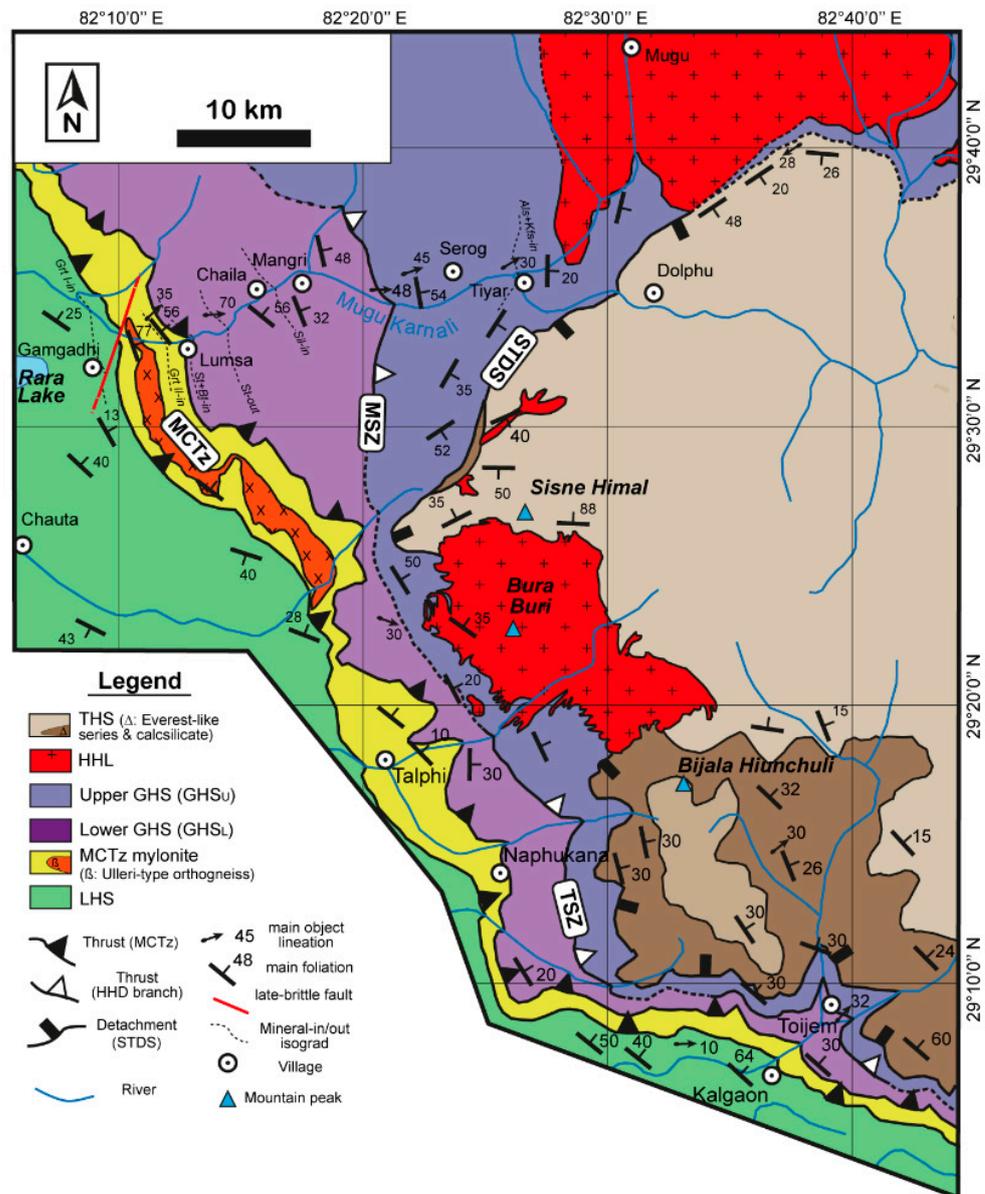

Figure 9. Geological map of Mugu Karnali and Lower Dolpo (western Nepal) [127].

Table 2. Summary of structural and geochronology data sets of the HHD in western Nepal and NW India [120,124,125,128].

Shear Zone and Locality	Tectonics Unit	Sheared Lithotypes	Strike & Dip of Mylonitic Foliation	Trend & Plunge of Lineation	Sense of Shear	Syn Shear Metamorphism	Deformation Mechanisms and Deformation T	Timing of Shearing	Monazite Features
Badrinath s.z. (NW India)	Greater Himalayan Sequence	sillimanite-garnet-bearing migmatitic gneiss [d]	moderately dipping to the NE, oriented WNW-ESE [d]	trending NE-SW and plunging toward the NE at low- to moderate angle [d]	top-to-the-SW [d]	Retrometamorphism from Amphibolite-facies, T~720–700 °C and P 0.80–0.65 GP [d]	GBM_II in quartz & chessboard extinction in quartz; T > 650° [d]	23–19 Ma [d]	Chemically homogeneous grains (high-Y+HREE), and zoned grains with a low-Y+HREE core and high-Y+HREE rim [d]
Mangri s.z. (Mugu Karnali, W Nepal)	Greater Himalayan Sequence	sillimanite-garnet-bearing migmatitic gneiss [a]	S2: moderately dipping to the NE, oriented NW-SE [a]	L2: trending from NE-SW to ENE-WSW moderately plunging to the NE or ENE [a]	top-to-the-WSW/ SW [a]	Retrometamorphism at Amphibolite-facies, T~720–690 °C and P 0.80–0.7 GP [a]	GBM_II & chessboard extinction in quartz; T > 650° [a]	25–18 Ma [a]	Chemically zoned with a low-Y+HREE core and high-Y+HREE rim [a]
Tojiem s.z. (W Nepal)	Greater Himalayan Sequence	sillimanite-garnet-bearing migmatitic gneiss [b]	S2: moderately dipping to the NE, oriented NW-SE [b]	L2: trending NE-SW and plunging at medium angle toward NE [b]	top-to-the-SW [b]	Retrometamorphism at Amphibolite-facies, T~700–600 °C and P 0.70–0.55 GP [b]	GBM_II in quartz; T > 650° [d]	26–17 Ma [b]	Chemically heterogeneous grains, in which cores yield older than the rims [b]
Chomrong Thrust (Central Nepal)	Greater Himalayan Sequence	kyanite-garnet-bearing migmatitic gneiss [c]	S2: moderately dipping to the NE, oriented NW-SE [c]	L2: trending NE-SW, shallowly or moderately plunging toward the NE [c]	top-to-the-SW [c]	Retrometamorphism from Amphibolite-facies, T~670–650° and P~0.8–0.7 GPa [c]	GBM_II in quartz & chessboard extinction in quartz T > 650° [c]	25–18 Ma [c]	Zoned grains with intermediate-Y core, low-Y+HREE mantle and high-Y+HREE rim [c]

[a]: Montomoli et al., 2013 & Iaccarino et al., 2017; [b]: Carosi et al., 2010; [c]: Iaccarino et al., 2015; [d]: Benetti et al., 2021.

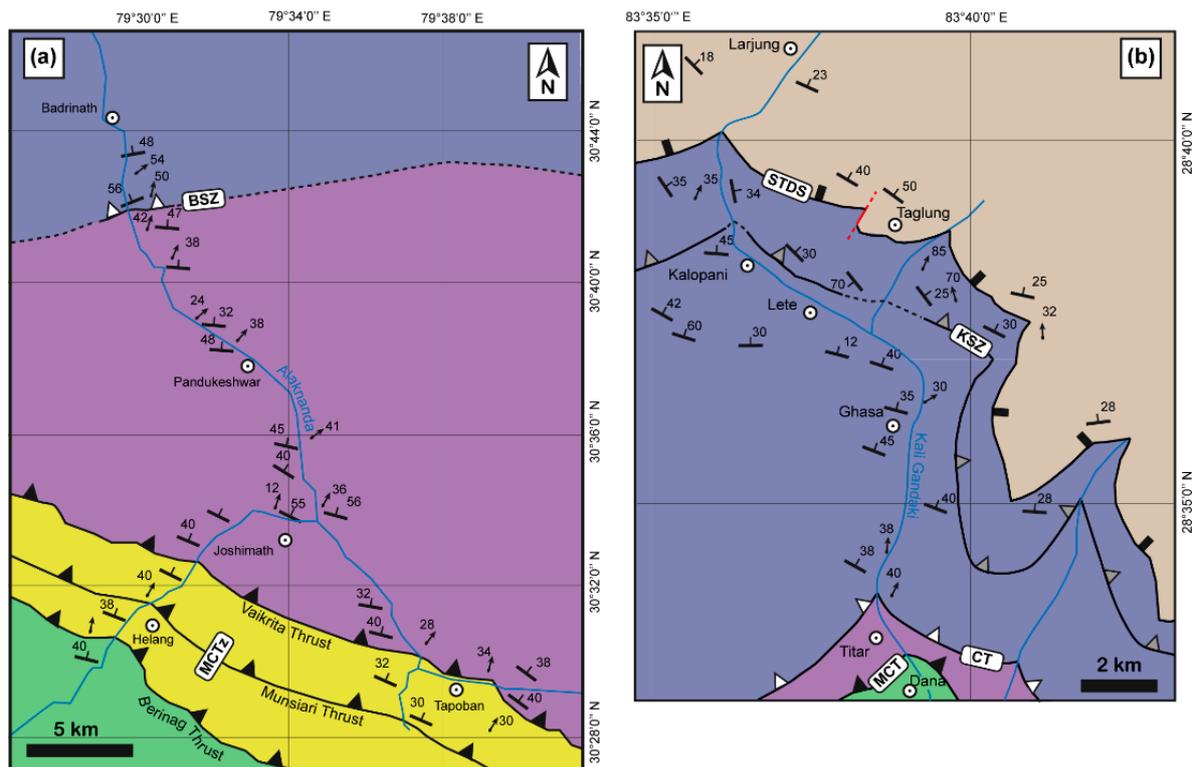**Figure 10.** (**a**) Geological map of NW India [128]; (**b**) geological map of central Nepal. Same legend as in Figure 9 [125].

The Badrinath Shear Zone rocks followed a clockwise path achieving a maximum pressure of 1.0 GPa and then re-equilibrated at peak conditions around 700–720 °C and 0.65–0.8 GPa (Figure 12). In situ U-Th-Pb dating on zoned monazites revealed that the Badrinath Shear Zone followed a prograde metamorphic path from 34 to 24 Ma, followed by decompression at c. 23 Ma in the sillimanite stability field, which continued at least until 19 Ma [128]. The Badrinath Shear Zone was responsible for a difference in pressure conditions (c. 0.2–0.3 GPa) and led to the onset of exhumation (c. 3 Ma earlier), between the upper GHS and the lower GHS [128].

The activity of the Mangri Shear Zone (western Nepal; Figure 9, Table 2) divided the GHS into two portions: an upper and a lower one [124]. It was associated with the decompression in the sillimanite stability field of the upper GHS rock package, showing relicts of relatively high-pressure metamorphism within the kyanite stability field. P-T conditions indicate that the final pattern due to the Mangri Shear Zone is that the footwall rocks record a higher pressure (1.0–0.9 GPa) than the hanging wall (0.7 GPa), at similar temperatures (675°–700 °C) (Figure 12). In situ LA-ICP-MS U–(Th)–Pb dating of zoned monazite in metapelites constrained the shearing related to retrograde high-Y monazite growth to between c. 25 and 18 Ma. Samples from the lower GHS experienced ductile shearing related to retrograde zoning in monazite (high-Y rims) later, only at <17–13 Ma. These ages and the associated P-T-t paths reveal that peak metamorphic conditions were reached c. 5–7 myr later in the footwall of the shear zone with respect to the hanging wall [121,124], pointing to a diachronism in the metamorphism triggered by the occurring Mangri Shear Zone. What is important here is to stress that, due to the shear zone activity, when the footwall rocks experienced prograde metamorphic conditions, associated with burial, the hanging wall rocks experienced decompression.
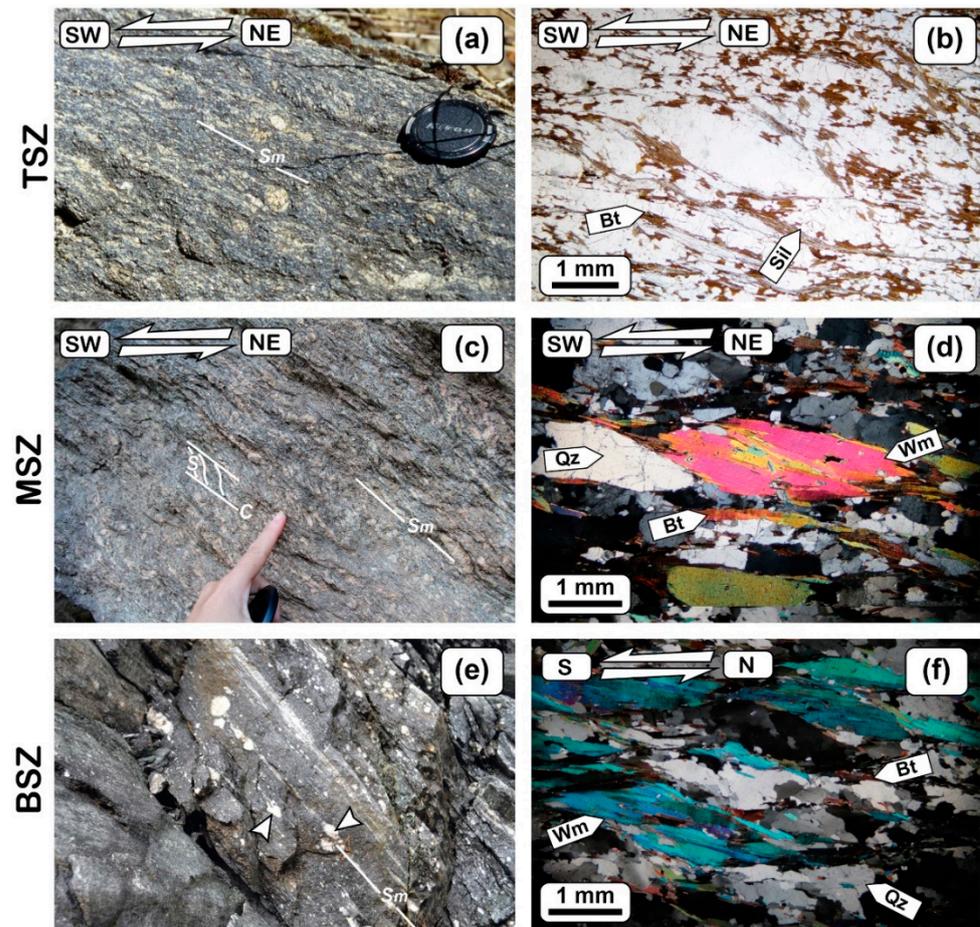
Figure 11. Meso- and microstructures of HHD mylonite pointing to a top-to-the-S/SW sense of shear (white arrows). Sm is the mylonitic foliation. (**a**) Sigma-type porphyroclasts in the Tojiem Shear Zone mylonite (Lower Dolpo, western Nepal) (coord. Lat. 29°08′32.6″ N—Long. 82°39′20.7″ E): mesoscale. (**b**) Sigma-type porphyroclast in the Tojiem Shear Zone mylonite: microscale with sillimanite and biotite along shear planes (Sm) (PPL). (**c**) S-C fabric in the Mangri Shear Zone (Mugu-Karnali valley; western Nepal) (coord. Lat. 29°34′31.30″ N—Long. 82°21′32.00″ E). (**d**) Biotite-foliation fish; Mangri Shear Zone (CPL). (**e**) Porphyroclasts in the Badrinath Shear Zone mylonite (Alaknanda valley; north-west India) (coord. Lat. 30°42′19.29″ N—Long. 79°30′12.14″). (**f**) Mica fish; Badrinath Shear Zone (CPL; FOV is 0.8 m). Mineral abbreviations as in Whitney and Evans (2010) [38].

In western Nepal, the activity of the Tojiem Shear Zone (Figures 2 and 9; Table 2) started at c. 26 Ma, constrained by in situ SHRIMP (sensitive high-resolution ion microprobe) monazite dating, coupled with LA-ICP-MS (laser ablation inductively coupled plasma mass spectrometry) trace element analyses on monazite in mylonites of the shear zone [120]. Monazite inside garnet exhibits older ages between c. 43 and 30 Ma that are related to prograde metamorphism during and following the collisional stage. The end of the shearing has been constrained by the age of an undeformed leucogranite dyke to c. 17 Ma, crosscutting the foliation. Geotermobarometry suggests that the Tojiem Shear Zone developed after the metamorphic peak, during the retrograde path of the sheared rocks: pressures of c. 0.9 GPa are recored in the footwall and 0.7 GPa in the hanging wall, with similar temperatures of 675–700 °C. Therefore, such a situation is comparable to the Mangri Shear Zone.
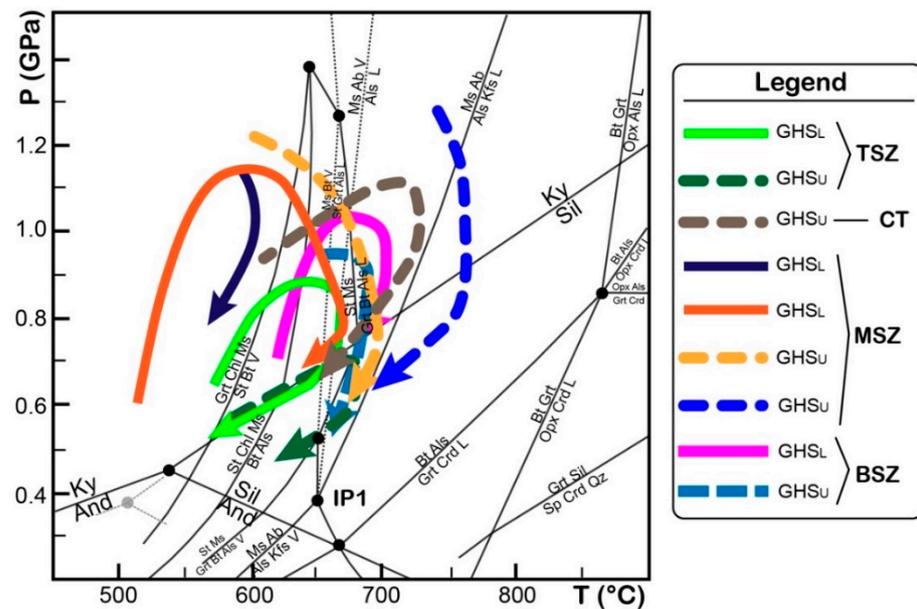
Figure 12. Summary of P-T paths of the different HHD branches discussed in the text. Note how the P-T paths of the GHSL (footwall of the HHD) are mainly in the kyanite stability field, whereas the paths of the GHSU (hanging wall of the HHD) fall in the sillimanite stability field after a former pressure peak in the kyanite field.

In the Kali Gandaki valley (central Nepal), in situ LA-ICP-MS monazite dating in kyanite-bearing migmatitic paragneiss allowed constraining the activity of the Chomrong Thrust (Figures 2 and 10b) to c. 25–18 Ma [125] (Table 2). Zoned monazites in Y and Th revealed that sheared rocks underwent prograde metamorphism, reaching partial melting within the kyanite stability field (710–720 °C/1.0–1.1 GPa) at c. 43 to 28 Ma. Melting occurred, during prograde metamorphism close to the maximum pressure, between c. 36 and 28 Ma [129]. When the Chomrong Thrust was active (c. 25 and 18 Ma), these rocks changed their P-T trajectory and underwent decompression associated with pervasive high-temperature shearing, reaching P-T conditions of 650–670 °C and 0.7–0.8 GPa [125,130] (Figure 12).

7. Discussion and Conclusions

The study of shear zones in recent years has mainly focused on the geometry, kinematics and deformation mechanisms of relatively small-scale shear zones [5,67]. The study of km-size or regional-scale shear zones is often hampered by incomplete geological records due to the lack of continuous outcrops, the difficulty in correlating different fragments or the same shear zone [23,94,116,127] due to the large distance separating them or to the occurrence of subsequent tectonic events. Once the geometry and the kinematics of a shear zone have been detected, the timing of shearing remains the main topic to be addressed due to the availability of different chronometers, and assessing the correct shearing age is often challenging. In this framework, tracing first-order lithospheric structures in ancient and modern collisional orogens is rather difficult due to the complex tectonic and metamorphic history of the orogens. An integrated multidisciplinary technique, including field mapping, structural analysis at different scales and geochronology or, better, petrochronology, represents a very useful tool to better unravel the tectonic evolution of regional-scale shear zones.

In the case of the EVSZ, a dextral, transpressive shear zone in the Variscan belt, we were able to correlate different strands of the same shear zone system from the Corsica–Sardinia block, through the Maures Massif, up to the External Crystalline Massifs in the Western Alps. This also provides new reliable constraints that should be considered for paleogeographic reconstructions. Furthermore, data documented that the EVSZ is not

a simple late Variscan (or even Permian) strike-slip shear zone developed sincronously along all the different strands, but rather a crustal-scale system of transpressive shear zones with a complex and progressive evolution over time. Some of the branches were activated earlier than others (e.g., the FMSZ in the Argentera Massif), and therefore they record a long deformation history, while the younger branches (e.g., the PASZ in northern Sardinia) record a relatively shorter history. In this view, Simonetti et al. (2020) [62] identified two main generations of branches: the first one started at c. 340–330 Ma, and the second one started at c. 320 Ma. It is worth noting that the older shear zones of the system are fully localized in the migmatitic crust. This suggests that between c. 330 and 320 Ma, the Variscan lower crust was weak and easier to deform because of the ongoing anatexis. A detailed investigation of other shear zones, potentially linked to the EVSZ, could lead to the recognition of other generations of shear zones and more complex architectures of a possible anastomosing pattern of ductile shear zones. An anastomosing pattern can in fact accommodate the compatibility problem caused by the pure shear component in the development of transpressional shear zones.

The integration of vorticity data with detailed monazite ages along transects of the FMSZ and PVSZ shows that deformation evolved from a pure-shear-dominated transpression towards a simple shear-dominated transpression, from 330/340 Ma to 305/300 Ma [62,67] (Table 1). This can be related to a change from nearly orthogonal collision during D1 to the progressive initiation and increasing curvature of the two regional-scale arcs in the Variscan belt (Ibero-Armorican Arc and the eastern arc delimited to the east by the EVSZ) [79]. By increasing the curvature of the arc over time, the slip along the flanks of the arc increased, and this is reflected by the increasing component of simple shear in the younger mylonites of the EVSZ in the segments of the FMSZ and PVSZ and by the dominant pure shear component detected in the older mylonites [62,67].

The case of the HHD in the metamorphic core of the Himalaya is even more puzzling because the regional extent of this shear zone was completely neglected in the literature until a few years ago, even if some isolated strands were identified in a few parts of the orogen. Moreover, by establishing the duration of the shearing at c. 10–11 Ma, it was possible to highlight the effect of this protracted activity on the P-T-t paths of the footwall and hanging wall of the HHD. They reached the maximum P-T condition diachronically, showing different timings of exhumation caused by the kinematics of the HHD. Last but not least, the correct dating of the HHD allows unequivocally separating it from the lower MCT (often mixed in the past literature) and contributing to better discussing the models of assembly and of exhumation of the metamorphic core.

An integrated technique, as described here, enables the detection of what is often referred to as "hidden" or "cryptic" tectono-metamorphic discontinuity with the mid-crust exposed in the GHS in western and central Nepal. It has been recognized in Mugu-Karnali, Lower Dolpo, the Kaligandaki valley and NW India as well as elsewhere along the orogen (e.g., [113,118,127,131]) (Figure 2). A key point here is the sense of shear, which is top-to-the-S/SW. Linking the mineral growth along the mylonitic foliation and in shear bands, the HHD is inferred to have been active during decompression, after peak metamorphism and related deformation (at least in the HHD hanging wall) and later retrograde metamorphism, of the deformed rocks within the sillimanite stability field (Figure 11a,b). It is worth noting that sillimanite grew along C' shear planes (Figure 11b), whereas kyanite occurs in microlithons, pointing to how the top-to-the-S/SW sense of shear is associated with decompression (Figure 12).

Monazite petrochronology constrains the timing of shearing to c. 28–27 and 17 Ma (Figure 13a) and provides direct timing constraints on both metamorphism and deformation [[127] with references]. The youngest monazite dates suggest that, for a duration of c. 11–10 Ma, the footwall moved downward while the hanging wall was simultaneously exhumed. The hanging wall underwent retrograde metamorphism and exhumation over a duration of c. 11–10 Ma before the footwall. The HHD was active for several m.y. and deeply affected the metamorphic history of the wall rocks. Movement on this shear zone

at 28–27–17 Ma caused a discontinuity in the metamorphic paths of the hanging wall and footwall rocks which, until that point, shared similar P-T-t paths, which indicates a remarkably different timing of exhumation (Figure 13b,c). The earlier exhumation of the hanging wall rocks was triggered by the activation of the contractional top-to-the-S/SW HHD (Figure 13b). Exhumation by thrusting and/or contractional shear zones in the GHS was possible due to the contemporaneous activity of erosion, extensional tectonics or even the thinning of the GHS caused by non-coaxial deformation [132].
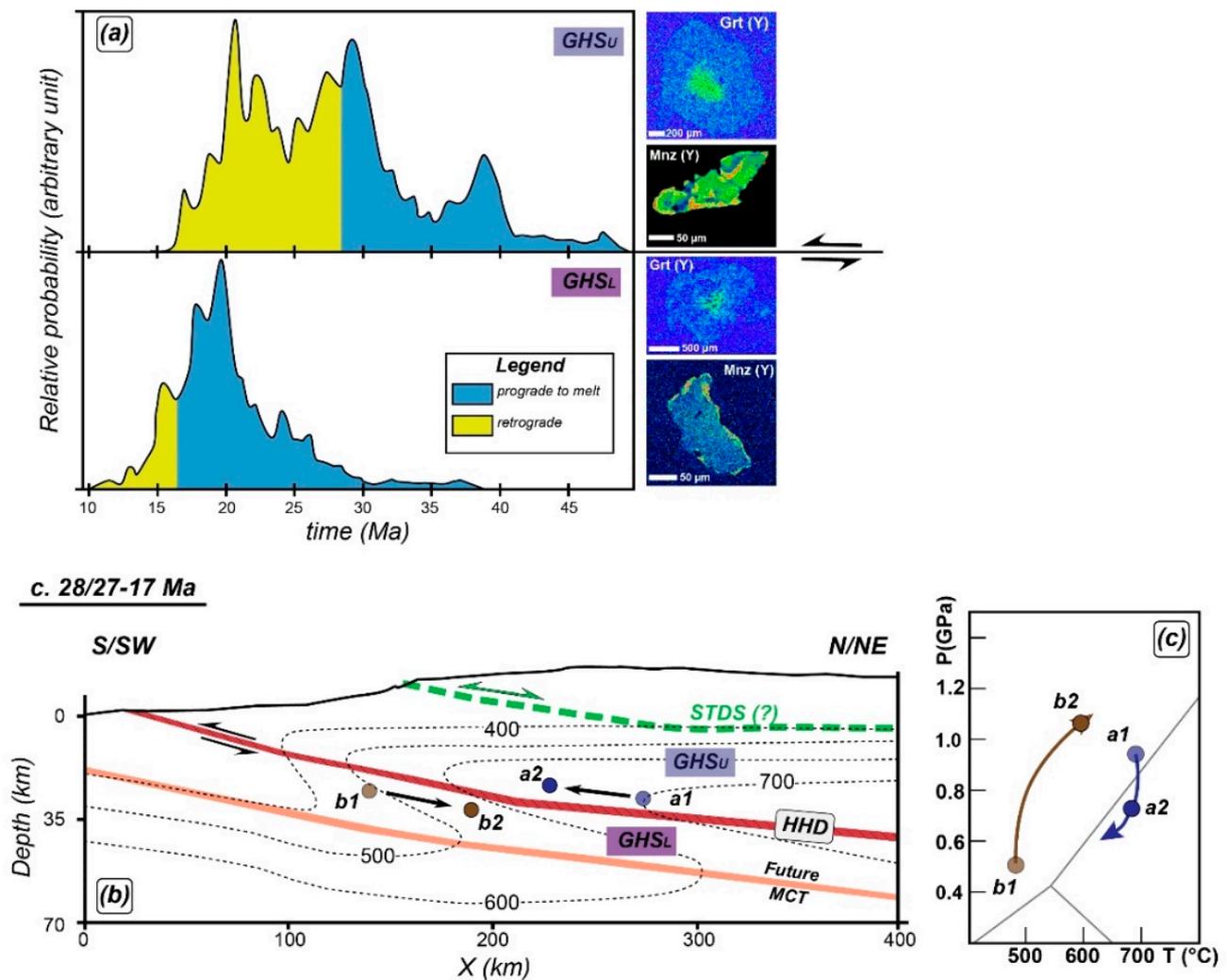

Figure 13. (**a**) Summary of metamorphic (prograde and retrograde) ages of the upper GHS (GHSU) and lower GHS (GHSL) for the Nepalese Himalaya (compilation modified from Wang et al., 2016 [131]). On the right are examples of X-ray maps showing common (and similar) Y zoning in garnet and monazite in the GHSU and GHSL (warm colors point to higher concentrations). (**b,c**) Model for the HHD shearing (in the time span of c. 28/27–17 Ma) affecting the GHS tectono-metamorphic history. (**c**) The HHD, due to its top-to-the-SW kinematics, triggered the earlier exhumation of the GHSU (dots a1 and a2 in (**c**)), while the GHSL was still experiencing prograde burial (dots b1 and b2 in (**c**)). Exhumation by the thrust-sense shear zone was possible due to a combination of the contemporaneous/episodic activity of the STDS, focused erosion in the frontal part of the belt and tectonic thinning of the GHS caused by non-coaxial flow.

Taking into account all of the common features of the recognized discontinuities in western-central Nepal up to Sikkim and Bhutan to the east, Montomoli et al. (2015) [116], Wang et al. (2016) [131] and Carosi et al. (2018; 2019) [127,130] correlated the discontinuities in the Himalaya along-strike length for ~1000 km (Figure 2). Benetti et al. (2021) [128], by

recognizing the Badrinath Shear Zone as a possible prosecution of the HHD to the NW, further stretched its occurrence up to ~1500 km along the strike of the belt.

Montomoli et al. (2015) [116] showed that deformation shifted in space and time from the HHD to the structurally lower MCT at c. 17 Ma. However, in order to unambiguously distinguish between the HHD and MCT, it is necessary to integrate structural, metamorphic and geochronological investigations of both hanging wall and footwall rocks and the intervening high-strain zone [113,116,120,121,124,125,127,131,133].

This framework agrees with the complex structural architecture of the GHS along the belt. The progressive exhumation of the GHS occurred due to activation of first-order ductile shear zones localized within the GHS, such as the HHD. Recent Ar/Ar datings of the upper MCT (Vaikrita Thrust: VT) and lower MCT (Munsiari Thrust: MT) in NW India [134,135] have allowed us to recognize two different timings of activity of these two shear zones at c. 9–8 Ma and c. 5–4 Ma, respectively.

Looking at the structural position, sense of shear and timing of the HHD, VT and MT, we can clearly delineate a tectonic framework characterized by a shifting of deformation from the (now) upper HHD to the (now) lower VT and subsequently the MT. The mode of propagation of deformation and exhumation of the GHS and LHS rocks further agrees with the in-sequence shearing model proposed thus far for the GHS by Benetti et al. (2021) [128], Carosi et al. (2018) [127], Montemagni et al. (2020) [135], Montemagni and Villa (2021) [136] and Montomoli et al. (2013) [124]. The subsequent activation of the MCT (VT) and the lower thrust (MT) progressively incorporates slices of the LHS into the belt. It is still unclear what causes the shift in deformation from the (now) upper shear zones to the (now) lower shear zones and why it happens. Iaccarino et al. (2015) [125] proposed that this shift could be linked to the hardening (due to cooling and melt crystallization) of hanging wall rocks, compared to the footwall rocks, the latter being warmer and weaker in the same span of time. What is important to note is that, when deformation shifts downward, the upper (older) shear zones become inactive, as testified by undeformed crosscutting granite dykes in the HHD or by the growth of static, post-tectonic, white mica in the MCT (VT). This tectonic framework highlights the occurrence and development of an asymmetric shear zone in an orogenic wedge propagating to the foreland in addition to the four types of evolution of symmetric shear zones proposed by Fossen and Cavalcante (2017) [5].

Studies of the HHD in the Himalaya and of the EVSZ in the southern Variscan belt are two examples of a detailed characterization of high-temperature shear zones localized in the mid-crust showing a regional extent, occurring in different tectonic settings (including ortogonal vs. oblique collision/indentation), and of Earth's history. Several main aspects remain to be further investigated, such as why deformation localizes along the HHD in the GHS of the Himalaya and along the EVSZ in the Variscan belt. Furthermore, the integration of structural geology (at a different scale), geochronology and/or petrochronology and petrology strongly contributes to better understanding their role in the evolution of two collisional belts and to better clarifying their importance for the tectonic mechanisms active during the deformation of the continental lithosphere.

Institutional Review Board Statement: Not applicable.

Informed Consent Statement: Not applicable.

References

1. Müller, W.; Aerden, D.; Halliday, A.N. Isotopic Dating of Strain Fringe Increments: Duration and Rates of Deformation in Shear Zones. *Science* **2000**, *288*, 2195–2198. [CrossRef] [PubMed]
2. Williams, M.L.; Jercinovic, M.J. Tectonic Interpretation of Metamorphic Tectonites: Integrating Compositional Mapping, Microstructural Analysis and in Situ Monazite Dating. *J. Metamorph. Geol.* **2012**, *30*, 739–752. [CrossRef]
3. Williams, M.L.; Jercinovic, M.J. Microprobe Monazite Geochronology: Putting Absolute Time into Microstructural Analysis. *J. Struct. Geol.* **2002**, *24*, 1013–1028. [CrossRef]
4. Passchier, C.W.; Trouw, R.A.J. *Microtectonics*, 2nd ed.; Springer: Berlin, Germany, 2005.
5. Fossen, H.; Cavalcante, G.C.G. Shear Zones—A Review. *Earth-Sci. Rev.* **2017**, *171*, 434–455. [CrossRef]
6. Di Vincenzo, G.; Carosi, R.; Palmeri, R. The Relationship between Tectono-Metamorphic Evolution and Argon Isotope Records in White Mica: Constraints from in Situ40Ar–39Ar Laser Analysis of the Variscan Basement of Sardinia. *J. Petrol.* **2004**, *45*, 1013–1043. [CrossRef]
7. Villa, I.M. Diffusion in Mineral Geochronometers: Present and Absent. *Chem. Geol.* **2016**, *420*, 1–10. [CrossRef]
8. Yund, R.A.; Tullis, J. Compositional Changes of Minerals Associated with Dynamic Recrystallizatin. *Contrib. Mineral. Petrol.* **1991**, *108*, 346–355. [CrossRef]
9. Villa, I.M.; Hermann, J.; Müntener, O.; Trommsdorff, V. 39Ar−40Ar Dating of Multiply Zoned Amphibole Generations (Malenco, Italian Alps). *Contrib. Mineral. Petrol.* **2000**, *140*, 363–381. [CrossRef]
10. Kohn, M.J. Metamorphic Chronology—A Tool for All Ages: Past Achievements and Future Prospects. *Am. Mineral.* **2016**, *101*, 25–42. [CrossRef]
11. Bianco, C.; Godard, G.; Halton, A.; Brogi, A.; Liotta, D.; Caggianelli, A. The Lawsonite-Glaucophane Blueschists of Elba Island (Italy). *Lithos* **2019**, *348–349*, 105198. [CrossRef]
12. Engi, M. Petrochronology Based on REE-Minerals: Monazite, Allanite, Xenotime, Apatite. *Rev. Mineral. Geochem.* **2017**, *83*, 365–418. [CrossRef]
13. Kohn, M.J.; Engi, M.; Lanari, P. *Petrochronology: Methods and Applications*; De Gruyter: Berlin, Germany, 2017; Volume 83.
14. Lanari, P.; Engi, M. On Metamorphic Mineral Assemblages. *Rev. Mineral. Geochem.* **2017**, *83*, 55–102. [CrossRef]
15. Foster, G.; Parrish, R.R.; Horstwood, M.S.A.; Chenery, S.; Pyle, J.; Gibson, H.D. The Generation of Prograde P–T–t Points and Paths; A Textural, Compositional, and Chronological Study of Metamorphic Monazite. *Earth Planet. Sci. Lett.* **2004**, *228*, 125–142. [CrossRef]
16. Gasser, D.; Bruand, E.; Rubatto, D.; Stüwe, K. The Behaviour of Monazite from Greenschist Facies Phyllites to Anatectic Gneisses: An Example from the Chugach Metamorphic Complex, Southern Alaska. *Lithos* **2012**, *134–135*, 108–122. [CrossRef]
17. Alcock, J.; Muller, P.D.; Jercinovic, M.J. Monazite Ages and Pressure-Temperature-Time Paths from Anatectites in the Southern Ruby Range, Montana, USA: Evidence for Delamination, Ultramafic Magmatism, and Rapid Uplift at ca. 1780 Ma. *Can. J. Earth Sci.* **2013**, *50*, 1069–1084. [CrossRef]
18. Massonne, H.J. Wealth of P-T-t Information in Medium-High Grade Metapelites: Example from the Jubrique Unit of the Betic Cordillera, S Spain. *Lithos* **2014**, *208*, 137–157. [CrossRef]
19. Palin, R.M.; Searle, M.P.; St-Onge, M.R.; Waters, D.J.; Roberts, N.M.W.; Horstwood, M.S.A.; Parrish, R.R.; Weller, O.M.; Chen, S.; Yang, J. Monazite Geochronology and Petrology of Kyanite- and Sillimanite-Grade Migmatites from the Northwestern Flank of the Eastern Himalayan Syntaxis. *Gondwana Res.* **2014**, *26*, 323–347. [CrossRef]
20. Faure, M.; Mézème, E.B.; Duguet, M.; Cartier, C.; Talbot, J.Y. Paleozoic Tectonic Evolution of Medio-Europa from the Example of the French Massif Central and Massif Armoricain. *J. Virtual Explor.* **2005**, *19*, 1–25. [CrossRef]
21. Corsini, M.; Rolland, Y. Late Evolution of the Southern European Variscan Belt: Exhumation of the Lower Crust in a Context of Oblique Convergence. *Comptes Rendus Geosci.* **2009**, *341*, 214–223. [CrossRef]
22. Guillot, S.; Ménot, R.P. Paleozoic Evolution of the External Crystalline Massifs of the Western Alps. *Comptes Rendus Geosci.* **2009**, *341*, 253–265. [CrossRef]
23. Simonetti, M.; Carosi, R.; Montomoli, C.; Cottle, J.M.; Law, R.D. Transpressive Deformation in the Southern European Variscan Belt: New Insights from the Aiguilles Rouges Massif (Western Alps). *Tectonics* **2020**, *39*, e2020TC006153. [CrossRef]
24. Weinberg, R.F. Himalayan Leucogranites and Migmatites: Nature, Timing and Duration of Anatexis. *J. Metamorph. Geol.* **2016**, *34*, 821–843. [CrossRef]
25. Pyle, J.M.; Spear, F.S. Yttrium Zoning in Garnet: Coupling of Major and Accessory Phases during Metamorphic Reactions. *Geol. Mater. Res.* **1999**, *1*, 708.
26. Pyle, J.M.; Spear, F.S. Four Generations of Accessory-Phase Growth in Low-Pressure Migmatites from SW New Hampshire. *Am. Mineral.* **2003**, *88*, 338–351. [CrossRef]

27. Dahl, P.S.; Terry, M.P.; Jercinovic, M.J.; Williams, M.L.; Hamilton, M.A.; Foland, K.A.; Clement, S.M.; Friberg, L.V.M. Electron Probe (Ultrachron) Microchronometry of Metamorphic Monazite: Unraveling the Timing of Polyphase Thermotectonism in the Easternmost Wyoming Craton (Black Hills, South Dakota). *Am. Mineral.* **2005**, *90*, 1712–1728. [CrossRef]

28. Dumond, G.; Goncalves, P.; Williams, M.L.; Jercinovic, M.J. Subhorizontal Fabric in Exhumed Continental Lower Crust and Implications for Lower Crustal Flow: Athabasca Granulite Terrane, Western Canadian Shield. *Tectonics* **2010**, *29*, TC2006. [CrossRef]

29. Foster, G.; Gibson, H.D.; Parrish, R.; Horstwood, M.; Fraser, J.; Tindle, A. Textural, Chemical and Isotopic Insights into the Nature and Behaviour of Metamorphic Monazite. *Chem. Geol.* **2002**, *191*, 183–207. [CrossRef]

30. Gibson, H.D.; Carr, S.D.; Brown, R.L.; Hamilton, M.A. Correlations between Chemical and Age Domains in Monazite, and Metamorphic Reactions Involving Major Pelitic Phases: An Integration of ID-TIMS and SHRIMP Geochronology with Y-Th-U X-ray Mapping. *Chem. Geol.* **2004**, *211*, 237–260. [CrossRef]

31. Janots, E.; Engi, M.; Berger, A.; Allaz, J.; Schwarz, J.-O.; Spandler, C. Prograde Metamorphic Sequence of REE Minerals in Pelitic Rocks of the Central Alps: Implications for Allanite–Monazite–Xenotime Phase Relations from 250 to 610 °C. *J. Metamorph. Geol.* **2008**, *26*, 509–526. [CrossRef]

32. Spear, F.S.; Pyle, J.M. Theoretical Modeling of Monazite Growth in a Low-Ca Metapelite. *Chem. Geol.* **2010**, *273*, 111–119. [CrossRef]

33. Kohn, M.J.; Wieland, M.S.; Parkinson, C.D.; Upreti, B.N. Five Generations of Monazite in Langtang Gneisses: Implications for Chronology of the Himalayan Metamorphic Core. *J. Metamorph. Geol.* **2005**, *23*, 399–406. [CrossRef]

34. Law, R.D. Deformation Thermometry Based on Quartz C-Axis Fabrics and Recrystallization Microstructures: A Review. *J. Struct. Geol.* **2014**, *66*, 129–161. [CrossRef]

35. Stipp, M.; Stünitz, H.; Heilbronner, R.; Schmid, S.M. Dynamic Recrystallization of Quartz: Correlation between Natural and Experimental Conditions. *Geol. Soc. Spec. Publ.* **2002**, *200*, 171–190. [CrossRef]

36. Tinkham, D.K.; Zuluaga, C.A.; Harold, H.S. Metapelite Phase Equilibria Modeling in MnNCKFMASH: The Effect of Variable Al$_2$O$_3$ and MgO/(MgO+FeO) on Mineral Sility. *Geol. Mater. Res.* **2001**, *3*, 1–42.

37. Spear, F.S. Monazite-Allanite Phase Relations in Metapelites. *Chem. Geol.* **2010**, *279*, 55–62. [CrossRef]

38. Whitney, D.L.; Evans, B.W. Abbreviations for Names of Rock-Forming Minerals. *Am. Mineral.* **2010**, *95*, 185–187. [CrossRef]

39. Yakymchuk, C.; Brown, M. Behaviour of Zircon and Monazite during Crustal Melting. *J. Geol. Soc.* **2014**, *171*, 465–479. [CrossRef]

40. Yakymchuk, C. Behaviour of Apatite during Partial Melting of Metapelites and Consequences for Prograde Suprasolidus Monazite Growth. *Lithos* **2017**, *274–275*, 412–426. [CrossRef]

41. Regis, D.; Warren, C.J.; Mottram, C.M.; Roberts, N.M.W. Using Monazite and Zircon Petrochronology to Constrain the P–T–t Evolution of the Middle Crust in the Bhutan Himalaya. *J. Metamorph. Geol.* **2016**, *34*, 617–639. [CrossRef]

42. Foster, G.; Parrish, R.R. Metamorphic Monazite and the Generation of P-T-t Paths. *Geol. Soc. Spec. Publ.* **2003**, *220*, 25–47. [CrossRef]

43. Mahan, K.H.; Goncalves, P.; Williams, M.L.; Jercinovic, M.J. Dating Metamorphic Reactions and Fluid Flow: Application to Exhumation of High-P Granulites in a Crustal-Scale Shear Zone, Western Canadian Shield. *J. Metamorph. Geol.* **2006**, *24*, 193–217. [CrossRef]

44. Shrestha, S.; Larson, K.P.; Duesterhoeft, E.; Soret, M.; Cottle, J.M. Thermodynamic Modelling of Phosphate Minerals and Its Implications for the Development of P-T-t Histories: A Case Study in Garnet—Monazite Bearing Metapelites. *Lithos* **2019**, *334–335*, 141–160. [CrossRef]

45. Larson, K.P.; Shrestha, S.; Cottle, J.M.; Guilmette, C.; Johnson, T.A.; Gibson, H.D.; Gervais, F. Re-Evaluating Monazite as a Record of Metamorphic Reactions. *Geosci. Front.* **2021**, *13*, 101340. [CrossRef]

46. Arthaud, F.; Matte, P. Late Paleozoic Strike-Slip Faulting in Southern Europe and Northern Africa: Result of a Right-Lateral Shear Zone between the Appalachians and the Urals. *Geol. Soc. Am. Bull.* **1977**, *88*, 1305–1320. [CrossRef]

47. Burg, J.P.; Matte, P.J. A Cross Section through the French Massif Central and the Scope of Its Variscan Geodynamic Evolution. *Z. Dtsch. Geol. Ges.* **1978**, *129*, 429–460. [CrossRef]

48. Tollmann, A. Grossräumiger Variszischer Deckenbau Im Moldanubikum Un Neue Gedanken Zum Variszikum Europas. *Geotecton. Res.* **1982**, *64*, 1–61.

49. Matte, P. The Variscan Collage and Orogeny (480–290 Ma) and the Tectonic Definition of the Armorica Microplate: A Review. *Terra Nova* **2001**, *13*, 122–128. [CrossRef]

50. Kroner, U.; Roscher, M.; Romer, R.L. Ancient Plate Kinematics Derived from the Deformation Pattern of Continental Crust: Paleo- and Neo-Tethys Opening Coeval with Prolonged Gondwana–Laurussia Convergence. *Tectonophysics* **2016**, *681*, 220–233. [CrossRef]

51. Fluck, P.; Piqué, A.; Schneider, J.-L.; Whitechurch, H. Le Socle Vosgien/The Vosgian Basement. *Sci. Géol. Bull. Mémoires* **1991**, *44*, 207–235. [CrossRef]

52. Ballèvre, M.; Bosse, V.; Ducassou, C.; Pitra, P. Palaeozoic History of the Armorican Massif: Models for the Tectonic Evolution of the Suture Zones. *Comptes Rendus Geosci.* **2009**, *341*, 174–201. [CrossRef]

53. Faure, M.; Lardeaux, J.M.; Ledru, P. A Review of the Pre-Permian Geology of the Variscan French Massif Central. *Comptes Rendus Geosci.* **2009**, *341*, 202–213. [CrossRef]

54. Skrzypek, E.; Tabaud, A.S.; Edel, J.B.; Schulmann, K.; Cocherie, A.; Guerrot, C.; Rossi, P. The Significance of Late Devonian Ophiolites in the Variscan Orogen: A Record from the Vosges Klippen Belt. *Int. J. Earth Sci.* **2012**, *101*, 951–972. [CrossRef]

55. Schulmann, K.; Konopásek, J.; Janoušek, V.; Lexa, O.; Lardeaux, J.M.; Edel, J.B.; Štípská, P.; Ulrich, S. An Andean Type Palaeozoic Convergence in the Bohemian Massif. *Comptes Rendus Geosci.* **2009**, *341*, 266–286. [CrossRef]

56. Matte, P. La Chaine Varisque Parmi Les Chaines Paleozoiques Peri Atlantiques, Modele d'evolution et Position des Grands Blocs Continentaux Au Permo-Carbonifere. *Bull. Soc. Géol. Fr.* **1986**, *2*, 9–24. [CrossRef]

57. Matte, P.H.; Ribeiro, A. Forme et orientation de l'ellipsoide de deformation dans la virgation Hercynienne de Galice. Relations avec le plissement et hypothesessur la genese de l'arc Ibero-Americain. *C. R. Acad. Sci. Paris* **1975**, *280*, 2825–2828.

58. Brun, J.P.; Burg, J.P. Combined Thrusting and Wrenching in the Ibero-Armorican Arc: A Corner Effect during Continental Collision. *Earth Planet. Sci. Lett.* **1982**, *61*, 319–332. [CrossRef]

59. Dias, R.; Ribeiro, A. The Ibero-Armorican Arc: A Collision Effect against an Irregular Continent? *Tectonophysics* **1995**, *246*, 113–128. [CrossRef]

60. Dias, R.; Ribeiro, A.; Romão, J.; Coke, C.; Moreira, N. A Review of the Arcuate Structures in the Iberian Variscides; Constraints and Genetic Models. *Tectonophysics* **2016**, *681*, 170–194. [CrossRef]

61. Fernández-Lozano, J.; Pastor-Galán, D.; Gutiérrez-Alonso, G.; Franco, P. New Kinematic Constraints on the Cantabrian Orocline: A Paleomagnetic Study from the Peñalba and Truchas Synclines, NW Spain. *Tectonophysics* **2016**, *681*, 195–208. [CrossRef]

62. Simonetti, M.; Carosi, R.; Montomoli, C.; Corsini, M.; Petroccia, A.; Cottle, J.M.; Iaccarino, S. Timing and Kinematics of Flow in a Transpressive Dextral Shear Zone, Maures Massif (Southern France). *Int. J. Earth Sci.* **2020**, *109*, 2261–2285. [CrossRef]

63. Simonetti, M.; Carosi, R.; Montomoli, C.; Langone, A.; D'Addario, E.; Mammoliti, E. Kinematic and Geochronological Constraints on Shear Deformation in the Ferriere-Mollières Shear Zone (Argentera-Mercantour Massif, Western Alps): Implications for the Evolution of the Southern European Variscan Belt. *Int. J. Earth Sci.* **2018**, *107*, 2163–2189. [CrossRef]

64. Bellot, J.-P. The Palaeozoic Evolution of the Maures Massif (France) and Its Potential Correlation with other Areas of the Variscan Belt: A Review. *Artic. J. Virtual Explor.* **2005**, *19*, 4. [CrossRef]

65. Ballèvre, M.; Manzotti, P.; Dal Piaz, G.V. Pre-Alpine (Variscan) Inheritance: A Key for the Location of the Future Valaisan Basin (Western Alps). *Tectonics* **2018**, *37*, 786–817. [CrossRef]

66. Carosi, R.; Montomoli, C.; Tiepolo, M.; Frassi, C. Geochronological Constraints on Post-Collisional Shear Zones in the Variscides of Sardinia (Italy). *Terra Nova* **2012**, *24*, 42–51. [CrossRef]

67. Carosi, R.; Petroccia, A.; Iaccarino, S.; Simonetti, M.; Langone, A.; Montomoli, C. Kinematics and Timing Constraints in a Transpressive Tectonic Regime: The Example of the Posada-Asinara Shear Zone (NE Sardinia, Italy). *Geosciences* **2020**, *10*, 288. [CrossRef]

68. Padovano, M.; Elter, F.M.; Pandeli, E.; Franceschelli, M. The East Variscan Shear Zone: New Insights into Its Role in the Late Carboniferous Collision in Southern Europe. *Int. Geol. Rev.* **2012**, *54*, 957–970. [CrossRef]

69. Padovano, M.; Dörr, W.; Elter, F.M.; Gerdes, A. The East Variscan Shear Zone: Geochronological Constraints from the Capo Ferro Area (NE Sardinia, Italy). *Lithos* **2014**, *196–197*, 27–41. [CrossRef]

70. García-Navarro, E.; Fernández, C. Final Stages of the Variscan Orogeny at the Southern Iberian Massif: Lateral Extrusion and Rotation of Continental Blocks. *Tectonics* **2004**, *23*, 1–20. [CrossRef]

71. Pereira, M.F.; Apraiz, A.; Silva, J.B.; Chichorro, M. Tectonothermal Analysis of High-Temperature Mylonitization in the Coimbra–Córdoba Shear Zone (SW Iberian Massif, Ouguela Tectonic Unit, Portugal): Evidence of Intra-Continental Transcurrent Transport during the Amalgamation of Pangea. *Tectonophysics* **2008**, *461*, 378–394. [CrossRef]

72. Tapponnier, P.; Molnar, P. Active Faulting and Tectonics in China. *J. Geophys. Res.* **1977**, *82*, 2905–2930. [CrossRef]

73. Tapponier, P.; Peltzer, G.; Le Dain, A.Y.; Armijo, R.; Cobbold, P. Propagating Extrusion Tectonics in Asia: New Insights from Simple Experiments with Plasticine. *Geology* **1982**, *10*, 611–616. [CrossRef]

74. Rosenbaum, G.; Lister, G.; Duboz, C. Reconstruction of the Tectonic Evolution of the Western Mediterranean since the Oligocene. *Virtual Explor.* **2002**, *8*, 6. [CrossRef]

75. Stampfli, G.M.; Borel, G.D.; Marchant, R.; Mosar, J. Western Alps Geological Constraints on Western Tethyan Reconstructions. *J. Virtual Explor.* **2002**, *8*, 77–106. [CrossRef]

76. Turco, E.; Macchiavelli, C.; Mazzoli, S.; Schettino, A.; Pierantoni, P.P. Kinematic Evolution of Alpine Corsica in the Framework of Mediterranean Mountain Belts. *Tectonophysics* **2012**, *579*, 193–206. [CrossRef]

77. Advokaat, E.L.; van Hinsbergen, D.J.J.; Maffione, M.; Langereis, C.G.; Vissers, R.L.M.; Cherchi, A.; Schroeder, R.; Madani, H.; Columbu, S. Eocene Rotation of Sardinia, and the Paleogeography of the Western Mediterranean Region. *Earth Planet. Sci. Lett.* **2014**, *401*, 183–195. [CrossRef]

78. Carosi, R.; Palmeri, R. Orogen-Parallel Tectonic Transport in the Variscan Belt of Northeastern Sardinia (Italy): Implications for the Exhumation of Medium-Pressure Metamorphic Rocks. *Geol. Mag.* **2002**, *139*, 497–511. [CrossRef]

79. Elter, F.M.; Musumeci, G.; Pertusati, P.C. Late Hercynian Shear Zones in Sardinia. *Tectonophysics* **1990**, *176*, 387–404. [CrossRef]

80. Iacopini, D.; Carosi, R.; Montomoli, C.; Passchier, C.W. Strain Analysis and Vorticity of Flow in the Northern Sardinian Variscan Belt: Recognition of a Partitioned Oblique Deformation Event. *Tectonophysics* **2008**, *446*, 77–96. [CrossRef]

81. Frassi, C.; Carosi, R.; Montomoli, C.; Law, R.D. Kinematics and Vorticity of Flow Associated with Post-Collisional Oblique Transpression in the Variscan Inner Zone of Northern Sardinia (Italy). *J. Struct. Geol.* **2009**, *31*, 1458–1471. [CrossRef]

82.　Graziani, R.; Montomoli, C.; Iaccarino, S.; Menegon, L.; Nania, L.; Carosi, R. Structural Setting of a Transpressive Shear Zone: Insights from Geological Mapping, Quartz Petrofabric and Kinematic Vorticity Analysis in NE Sardinia (Italy). *Geol. Mag.* **2020**, *157*, 1898–1916. [CrossRef]

83.　Cruciani, G.; Franceschelli, M.; Massonne, H.-J.; Carosi, R.; Montomoli, C. Pressure–temperature and deformational evolution of high-pressure metapelites from Variscan Ne Sardinia, Italy. *Lithos* **2013**, *175–176*, 272–284. [CrossRef]

84.　Cruciani, G.; Franceschelli, M.; Groppo, C.; Oggiano, G.; Spano, M.E. Re-Equilibration History and P–T Path of Eclogites from Variscan Sardinia, Italy: A Case Study from the Medium-Grade Metamorphic Complex. *Int. J. Earth Sci.* **2015**, *104*, 797–814. [CrossRef]

85.　Scodina, M.; Cruciani, G.; Franceschelli, M. Metamorphic Evolution and P–T Path of the Posada Valley Amphibolites: New Insights on the Variscan High Pressure Metamorphism in NE Sardinia, Italy. *Comptes Rendus Geosci.* **2021**, *353*, 227–246. [CrossRef]

86.　Schneider, J.; Corsini, M.; Reverso-Peila, A.; Lardeaux, J.M. Thermal and Mechanical Evolution of an Orogenic Wedge during Variscan Collision: An Example in the Maures–Tanneron Massif (SE France). *Geol. Soc. Lond. Spec. Publ.* **2014**, *405*, 313–331. [CrossRef]

87.　Gerbault, M.; Schneider, J.; Reverso-Peila, A.; Corsini, M. Crustal Exhumation during Ongoing Compression in the Variscan Maures-Tanneron Massif, France-Geological and Thermo-Mechanical Aspects. *Tectonophysics* **2018**, *746*, 439–458. [CrossRef]

88.　Musumeci, G.; Colombo, F. Late Visean Mylonitic Granitoids in the Argentera Massif (Western Alps, Italy): Age and Kinematic Constraints on the Ferrière–Mollières Shear Zone. *Comptes Rendus Geosci.* **2002**, *334*, 213–220. [CrossRef]

89.　Rubatto, D.; Schaltegger, U.; Lombardo, D.; Colombo, F.; Compagnoni, R. Complex Paleozoic Magmatic and Metamorphic Evolution in the Argentera Massif (Western Alps). *Schweiz. Mineral. Petrogr. Mitt.* **2001**, *81*, 213–228.

90.　Rubatto, D.; Ferrando, S.; Compagnoni, R.; Lombardo, B. Carboniferous High-Pressure Metamorphism of Ordovician Protoliths in the Argentera Massif (Italy), Southern European Variscan Belt. *Lithos* **2010**, *116*, 65–76. [CrossRef]

91.　Jouffray, F.; Spalla, M.I.; Lardeaux, J.M.; Filippi, M.; Rebay, G.; Corsini, M.; Zanoni, D.; Zucali, M.; Gosso, G. Variscan Eclogites from the Argentera–Mercantour Massif (External Crystalline Massifs, SW Alps): A Dismembered Cryptic Suture Zone. *Int. J. Earth Sci.* **2020**, *109*, 1273–1294. [CrossRef]

92.　Bussy, F.; Péronnet, V.; Ulianov, A.; Epard, J.L.; von Raumer, J.F. Ordovician Magmatism in the External French Alps: Witness of a Peri-Gondwanan Active Continental Margin. *Ordovician World* **2011**, *14*, 567–574.

93.　Vanardois, J.; Roger, F.; Trap, P.; Goncalves, P.; Lanari, P.; Paquette, J.-L.; Marquer, D.; Cagnard, F.; Le Bayon, B.; Melleton, J.; et al. Exhumation of Deep Continental Crust in a Transpressive Regime: The Example of Variscan Eclogites from the Aiguilles-Rouges Massif (Western Alps). *J. Metamorph. Geol.* **2022**, 1–34. [CrossRef]

94.　Simonetti, M.; Carosi, R.; Montomoli, C.; Law, R.D.; Cottle, J.M. Unravelling the Development of Regional-Scale Shear Zones by a Multidisciplinary Approach: The Case Study of the Ferriere-Mollières Shear Zone (Argentera Massif, Western Alps). *J. Struct. Geol.* **2021**, *149*, 104399. [CrossRef]

95.　Fossen, H. *Structural Geology*; Cambridge University Press: Cambridge, UK, 2016.

96.　Carosi, R.; D'Addario, E.; Mammoliti, E.; Montomoli, C.; Simonetti, M. Geology of the Northwestern Portion of the Ferriere-Mollieres Shear Zone, Argentera Massif, Italy. *J. Maps* **2016**, *12*, 466–475. [CrossRef]

97.　Genier, F.; Bussy, F.; Epard, J.L.; Baumgartner, L. Water-Assisted Migmatization of Metagraywackes in a Variscan Shear Zone, Aiguilles-Rouges Massif, Western Alps. *Lithos* **2008**, *102*, 575–597. [CrossRef]

98.　Oliot, E.; Melleton, J.; Schneider, J.; Corsini, M.; Gardien, V.; Yann, R. Variscan Crustal Thickening in the Maures-Tanneron Massif (South Variscan Belt, France): New in Situ Monazite U-Th-Pb Chemical Dating of High-Grade Rocks. *Bull. Soc. Géol. Fr.* **2015**, *186*, 145–169. [CrossRef]

99.　Grandjean, V.; Guillot, S.; Pecher, A. A New Record of the LP-HT Late-Variscan Metamorphism: The Peyre-Arguet Unit (Haut-Dauphine). *Comptes Rendus L'Acad. Sci. Ser. Fasc. Sci. Terre Planetes* **1996**, *322*, 189–195.

100.　Hu, X.; Garzanti, E.; Wang, J.; Huang, W.; An, W.; Webb, A. The Timing of India-Asia Collision Onset—Facts, Theories, Controversies. *Earth-Sci. Rev.* **2016**, *160*, 264–299. [CrossRef]

101.　Montomoli, C.; Carosi, R.; Rubatto, D.; Visonà, D.; Iaccarino, S. Tectonic Activity along the Inner Margin of the South Tibetan Detachment Constrained by Syntectonic Leucogranite Emplacement in Western Bhutan. *Ital. J. Geosci.* **2017**, *136*, 5–14. [CrossRef]

102.　Gansser, A. *Geology of the Himalayas*; Interscience: New York, NY, USA, 1964.

103.　Searle, M.P.; Law, R.D.; Godin, L.; Larson, K.P.; Streule, M.J.; Cottle, J.M.; Jessup, M.J. Defining the Himalayan Main Central Thrust in Nepal. *J. Geol. Soc.* **2008**, *165*, 523–534. [CrossRef]

104.　Iaccarino, S.; Montomoli, C.; Carosi, R.; Montemagni, C.; Massonne, H.J.; Langone, A.; Jain, A.K.; Visonà, D. Pressure-Temperature-Deformation-Time Constraints on the South Tibetan Detachment System in the Garhwal Himalaya (NW India). *Tectonics* **2017**, *36*, 2281–2304. [CrossRef]

105.　Burg, J.P.; Chen, G.M. Tectonics and Structural Zonation of Southern Tibet, China. *Nature* **1984**, *311*, 219–223. [CrossRef]

106.　Burchfiel, B.C.; Chen, Z.; Hodges, K.V.; Liu, Y.; Royden, L.H.; Changrong, D.; Xu, L. The South Tibetan Detachment System, Himalayan Orogen: Extension Contemporaneous with and Parallel to Shortening in a Collisional Mountain Belt. *Spec. Pap. Geol. Soc. Am.* **1992**, *269*, 1–41. [CrossRef]

107.　Searle, M.P.; Godin, L. The South Tibetan Detachment and the Manaslu Leucogranite: A Structural Reinterpretation and Restoration of the Annapurna-Manaslu Himalaya, Nepal. *J. Geol.* **2003**, *111*, 505–523. [CrossRef]

108. Ambrose, T.K.; Larson, K.P.; Guilmette, C.; Cottle, J.M.; Buckingham, H.; Rai, S. Lateral Extrusion, Underplating, and out-of-Sequence Thrusting within the Himalayan Metamorphic Core, Kanchenjunga, Nepal. *Lithosphere* **2015**, *7*, 441–464. [CrossRef]

109. Hodges, K.V.; Parrish, R.R.; Searle, M.P. Tectonic Evolution of the Central Annapurna Range, Nepalese Himalayas. *Tectonics* **1996**, *15*, 1264–1291. [CrossRef]

110. Beaumont, C.; Jamieson, R.A.; Nguyen, M.H.; Lee, B. Himalayan Tectonics Explained by Extrusion of a Low-Viscosity Crustal Channel Coupled to Focused Surface Denudation. *Nature* **2001**, *414*, 738–742. [CrossRef]

111. Grujic, D.; Casey, M.; Davidson, C.; Hollister, L.S.; Kündig, R.; Pavlis, T.; Schmid, S. Ductile Extrusion of the Higher Himalayan Crystalline in Bhutan: Evidence from Quartz Microfabrics. *Tectonophysics* **1996**, *260*, 21–43. [CrossRef]

112. Godin, L.; Grujic, D.; Law, R.D.; Searle, M.P. Channel Flow, Ductile Extrusion and Exhumation in Continental Collision Zones: An Introduction. *Geol. Soc. Spec. Publ.* **2006**, *268*, 1–23. [CrossRef]

113. Cottle, J.M.; Larson, K.P.; Kellett, D.A. How Does the Mid-Crust Accommodate Deformation in Large, Hot Collisional Orogens? A Review of Recent Research in the Himalayan Orogen. *J. Struct. Geol.* **2015**, *78*, 119–133. [CrossRef]

114. Webb, A.G.; Yin, A.; Harrison, T.M.; Célérier, J.; Burgess, W.P. The Leading Edge of the Greater Himalayan Crystalline Complex Revealed in the NW Indian Himalaya: Implications for the Evolution of the Himalayan Orogen. *Geology* **2007**, *35*, 955–958. [CrossRef]

115. Kohn, M.J. P-T-t Data from Central Nepal Support Critical Taper and Repudiate Large-Scale Channel Flow of the Greater Himalayan Sequence. *Geol. Soc. Am. Bull.* **2008**, *120*, 259–273. [CrossRef]

116. Montomoli, C.; Carosi, R.; Iaccarino, S. Tectonometamorphic Discontinuities in the Greater Himalayan Sequence: A Local or a Regional Feature? *Geol. Soc. Lond. Spec. Publ.* **2015**, *412*, 25–41. [CrossRef]

117. Kaneko, Y. Two-Step Exhumation Model of the Himalayan Metamorphic Belt, Central Nepal. *J. Geol. Soc. Jpn.* **1997**, *103*, 203–226. [CrossRef]

118. Hodges, K.V. Tectonics of the Himalaya and Southern Tibet from Two Perspectives. *Geol. Soc. Am. Bull.* **2000**, *112*, 324–350. [CrossRef]

119. Waters, D.J. Metamorphic Constraints on the Tectonic Evolution of the High Himalaya in Nepal: The Art of the Possible. *Geol. Soc. Lond. Spec. Publ.* **2019**, *483*, 325–375. [CrossRef]

120. Carosi, R.; Montomoli, C.; Rubatto, D.; Visonà, D. Late Oligocene High-Temperature Shear Zones in the Core of the Higher Himalayan Crystallines (Lower Dolpo, Western Nepal). *Tectonics* **2010**, *29*, TC4029. [CrossRef]

121. Iaccarino, S.; Montomoli, C.; Carosi, R.; Massonne, H.J.; Visonà, D. Geology and Tectono-Metamorphic Evolution of the Himalayan Metamorphic Core: Insights from the Mugu Karnali Transect, Western Nepal (Central Himalaya). *J. Metamorph. Geol.* **2017**, *35*, 301–325. [CrossRef]

122. Vannay, J.C.; Hodges, K.V. Tectonometamorphic Evolution of the Himalayan Metamorphic Core between the Annapurna and Dhaulagiri, Central Nepal. *J. Metamorph. Geol.* **1996**, *14*, 635–656. [CrossRef]

123. Carosi, R.; Montomoli, C.; Visonà, D. A Structural Transect in the Lower Dolpo: Insights on the Tectonic Evolution of Western Nepal. *J. Asian Earth Sci.* **2007**, *29*, 407–423. [CrossRef]

124. Montomoli, C.; Iaccarino, S.; Carosi, R.; Langone, A.; Visonà, D. Tectonometamorphic Discontinuities within the Greater Himalayan Sequence in Western Nepal (Central Himalaya): Insights on the Exhumation of Crystalline Rocks. *Tectonophysics* **2013**, *608*, 1349–1370. [CrossRef]

125. Iaccarino, S.; Montomoli, C.; Carosi, R.; Massonne, H.J.; Langone, A.; Visonà, D. Pressure-Temperature-Time-Deformation Path of Kyanite-Bearing Migmatitic Paragneiss in the Kali Gandaki Valley (Central Nepal): Investigation of Late Eocene-Early Oligocene Melting Processes. *Lithos* **2015**, *231*, 103–121. [CrossRef]

126. Parsons, A.J.; Law, R.D.; Searle, M.P.; Phillips, R.J.; Lloyd, G.E. Geology of the Dhaulagiri-Annapurna-Manaslu Himalaya, Western Region, Nepal. 1:200,000. *J. Maps* **2016**, *12*, 100–110. [CrossRef]

127. Carosi, R.; Montomoli, C.; Iaccarino, S. 20 Years of Geological Mapping of the Metamorphic Core across Central and Eastern Himalayas. *Earth-Sci. Rev.* **2018**, *177*, 124–138. [CrossRef]

128. Benetti, B.; Montomoli, C.; Iaccarino, S.; Langone, A.; Carosi, R. Mapping Tectono-Metamorphic Discontinuities in Orogenic Belts: Implications for Mid-Crust Exhumation in NW Himalaya. *Lithos* **2021**, *392–393*, 106129. [CrossRef]

129. Carosi, R.; Montomoli, C.; Langone, A.; Turina, A.; Cesare, B.; Iaccarino, S.; Fascioli, L.; Visonà, D.; Ronchi, A.; Rai, S.M. Eocene Partial Melting Recorded in Peritectic Garnets from Kyanite-Gneiss, Greater Himalayan Sequence, Central Nepal. *Geol. Soc. Lond. Spec. Publ.* **2015**, *412*, 111–129. [CrossRef]

130. Carosi, R.; Montomoli, C.; Iaccarino, S.; Visonà, D. Structural Evolution, Metamorphism and Melting in the Greater Himalayan Sequence in Central-Western Nepal. *Geol. Soc. Lond. Spec. Publ.* **2019**, *483*, 305–323. [CrossRef]

131. Wang, J.M.; Zhang, J.J.; Liu, K.; Zhang, B.; Wang, X.X.; Rai, S.M.; Scheltens, M. Spatial and Temporal Evolution of Tectonometa-morphic Discontinuities in the Central Himalaya: Constraints from P-T Paths and Geochronology. *Tectonophysics* **2016**, *679*, 41–60. [CrossRef]

132. Long, S.P.; Kohn, M.J. Distributed ductile thinning during thrust emplacement: A commonly overlooked exhumation mechanism. *Geology* **2020**, *48*, 368–373. [CrossRef]

133. Carosi, R.; Montomoli, C.; Iaccarino, S.; Massonne, H.J.; Rubatto, D.; Langone, A.; Gemignani, L.; Visonà, D. Middle to Late Eocene Exhumation of the Greater Himalayan Sequence in the Central Himalayas: Progressive Accretion from the Indian Plate. *Geol. Soc. Am. Bull.* **2016**, *128*, 1571–1592. [CrossRef]

134. Montemagni, C.; Montomoli, C.; Iaccarino, S.; Carosi, R.; Jain, A.K.; Massonne, H.J.; Villa, I.M. Dating Protracted Fault Activities: Microstructures, Microchemistry and Geochronology of the Vaikrita Thrust, Main Central Thrust Zone, Garhwal Himalaya, NW India. *Geol. Soc. Lond. Spec. Publ.* **2018**, *481*, 127–146. [CrossRef]

135. Montemagni, C.; Carosi, R.; Fusi, N.; Iaccarino, S.; Montomoli, C.; Villa, I.M.; Zanchetta, S. Three-dimensional Vorticity and Time-constrained Evolution of the Main Central Thrust Zone, Garhwal Himalaya (NW India). *Terra Nova* **2020**, *32*, 215–224. [CrossRef]

136. Montemagni, C.; Villa, I.M. Geochronology of Himalayan Shear Zones: Unravelling the Timing of Thrusting from Structurally Complex Fault Rocks. *J. Geol. Soc.* **2021**, *178*, 235. [CrossRef]